Order Number 9010884

Nonequilibrium excitations in superconducting aluminum and high temperature superconducting devices

Hilton, Gene Charles, Ph.D.

University of Illinois at Urbana-Champaign, 1989

U·M·I
300 N. Zeeb Rd.
Ann Arbor, MI 48106

NON-EQUILIBRIUM EXCITATIONS IN SUPERCONDUCTING ALUMINUM AND HIGH TEMPERATURE SUPERCONDUCTING DEVICES

BY

GENE CHARLES HILTON

B.S., University of Tulsa, 1981

THESIS

Submitted in partial fulfillment of the requirements
for the degree of Doctor of Philosophy in Physics
in the Graduate College of the
University of Illinois at Urbana-Champaign, 1989

Urbana, Illinois

UNIVERSITY OF ILLINOIS AT URBANA-CHAMPAIGN

THE GRADUATE COLLEGE

AUGUST 1989

WE HEREBY RECOMMEND THAT THE THESIS BY

GENE CHARLES HILTON

ENTITLED NON-EQUILIBRIUM EXCITATIONS IN SUPERCONDUCTING ALUMINUM AND HIGH TEMPERATURE SUPERCONDUCTING DEVICES

BE ACCEPTED IN PARTIAL FULFILLMENT OF THE REQUIREMENTS FOR THE DEGREE OF DOCTOR OF PHILOSOPHY

Director of Thesis Research

Head of Department

Committee on Final Examination†

Chairperson

† Required for doctor's degree but not for master's.

O-517

NON-EQUILIBRIUM EXCTIATIONS IN SUPERCONDUCTING ALUMINUM
AND HIGH TEMPERATURE SUPERCONDUCTING DEVICES

Gene Charles Hilton, Ph.D.
Department of Physics
University of Illinois at Urbana-Champaign, 1989
Dale J. Van Harlingen, Advisor

This thesis describes work done in two separate areas of the field of superconductivity. The first part describes experiments performed to measure a predicted, but previously unmeasured non-equilibrium effect in superconducting aluminum. A charge imbalance, or charging of the normal fluid with respect to the superfluid, is generated by the interaction of an electric field and a supercurrent. We have shown that this effect does occur, however the measured temperature dependence of this effect does not agree with existing theory. In the second part of this thesis we report on efforts to make simple superconductor devices from the high-T_c ceramic oxide superconductors. We have made thin films of both $YBa_2Cu_3O_{7-x}$ and BiSrCaCuO by several methods, and measurements of bulk film properties are presented. These films have been patterned into different structures in a number of ways, including an *in-situ* ion milling modification technique. Data on these devices, and grain-boundary SQUIDS are presented.

ACKNOWLEDGMENTS

I would have never been able to complete the work described here without the assistance and support of a great many people. Dale Van Harlingen has been the best thesis advisor imaginable - knowledgeable, patient, and supportive. Also high on the list is my fellow group members. Ron Wakai, Kendall Springer, Fred Sharifi, Jorge Gavilano and Jonas Zmuidzinas have been great guys to be around the lab with, and have helped me in ways too numerous too mention. Ralph Schweinfurth, Ed Harris, and Alan Smith helped a lot on much of the high-T_c work, and never complained about all the lousy jobs that I gave them.

Much of this work would have been a great deal more difficult without the friendly and knowledgeable help of the MRL support staff. I would certainly like to acknowledge Bud Dittman in the machine shop, everyone in the storeroom, Donna Jacobs in the business office, and Jeff Zeigler in PES, for putting up with my "I need it yesterday" pleadings. Also of great assistance has been John Woodhouse and the entire staff of the Center for Microanalysis of Materials, and Tim Brock and John Hughes of the Microelectronics Center.

There are also many friends I wish to acknowledge. Though they didn't contribute to the work, they helped me keep my sanity and well being. I am grateful for the friendship of my fellow graduate students Dave Smith, Doug Smith, Dick Fink, Phil First, Matt Kim, and Dan Wright. All the musicians I have played with over the years have given me the best hobby in the world, particularly John Poelker, Margaret Shield, Dennis Youn, John Dietterich, Rob Sweeney, and Greg Robbins. John

Crilly, Daria Scatton, Sue Corcoran, and Angie Rolfs have been great bandmates, but have also given me so much more with their friendship.

Finally I would like to thank my parents, my brother and sisters, and of course, Donna Hurley. Without their love, support, and encouragement, none of this would have been possible.

This work has been supported by National Science Foundation Materials Research Program grant no. DMR 86 12860, and by the National Science Foundation Science and Technology Center grant no. DMR 88 9854. I would also like to acknowledge the Exxon Graduate Fellowship I had during my first year of graduate school, and the Physics Department Fellowship that I had during my last summer.

TABLE OF CONTENTS

Chapter 1

INTRODUCTION

Superconductivity has always been a field of great promise, both scientifically and technologically. Scientifically, the search for an explanation of superconductivity greatly advanced the state of condensed matter physics, and greatly enhanced the understanding of collective behavior in other systems. The search for new superconductors has had a large impact on material science, and the development of experimental techniques for superconductivity research has advanced other fields. Technologically, the promise of superconductivity is yet largely unfulfilled, although the discovery of the high temperatures ceramic oxides may change this. This thesis reflects some of this dual character.

The work described in the first part of this thesis describes measurements done on non-equilibrium excitations in superconducting aluminum. Specifically, we measured the theoretically predicted generation of an excitation called charge imbalance by the interaction of an electric field and a supercurrent. Charge imbalance is an excitation in which there is an excess of hole-like or electron-like quasiparticles in a superconductor. Quasiparticles are the elementary excitations in superconductors, and unlike electrons or holes in normal metals, reflect the many-body nature of the superconducting state. The effect we studied is predicted by a set of transport equations, similar to those

governing electrical conduction, thermal conduction, and the thermoelectric effect in a normal metal. However, it is one of many transport modes predicted that have no analog in normal metals. Only a few of these have been studied.

The second part of this thesis describes efforts to make simple thin-film superconducting devices out of the recently discovered high-T_c ceramic oxide superconductors. We decided to undertake this work because of the obvious scientific, and perhaps technological importance of these materials, and because there is a unique combination of capabilities available for some aspects of this work at the University of Illinois. Because the discovery of these materials is so recent, much of the work described is of a technological nature. It is important to learn how to make good thin-film samples before meaningful scientific measurements can be performed.

The outline of this thesis is as follows. Chapter 2 introduces some basic theoretical concepts in superconductivity and superconductor devices that are common to both topics studied. It starts with a review of the microscopic theory of Bardeen, Cooper, and Schrieffer, aimed at developing an understanding of quasiparticles. Aspects of Ginzburg-Landau phenomenological theory are then presented. Finally key concepts in the areas of Josephson junctions, weak links, and superconducting quantum-interference devices (SQUIDs) are given.

Chapter 3 presents the non-equilibrium work described above. First the non-equilibrium excitation modes of superconductors are described, as well as the transport equations governing the generation of these mode. Details of the generation, detection and relaxation of charge imbalance

are considered. We then discuss the experimental details, including sample fabrication and measurement techniques. The results obtained are then presented.

In the fourth chapter we discuss the work done on the high-T_c materials. After a brief overview of the field, details of fabrication of both $YBa_2Cu_3O_{7-x}$ and BiSrCaCuO thin films by several methods are presented. Measurements and comparisons between the different types of films is also given. Next, the different methods used to pattern these films into various structures is addressed. We then present results obtained using an *in-situ* ion milling process used to modify the samples, as well as measurements made on grain boundary SQUIDs.

Chapter 2

CONCEPTS IN SUPERCONDUCTIVITY

In this chapter we review some of the important theoretical points of superconductors, junctions and weak-links. The first part of this chapter is an overview of the theory of Bardeen, Cooper, and Schrieffer (BCS) aimed toward explaining excitations in superconductors, particularly quasiparticles. The next section deals with the Ginzburg-Landau phenomenological theory, to develop some concepts necessary to understand junctions and SQUIDs. Next we review the Josephson effect and other important concepts of weak-links and junctions. Lastly Superconducting Quantum-Interference Devices (SQUIDs) are examined.

2.1 The BCS Theory

In 1957, BCS [1] gave the first microscopic explanation for superconductivity, a phenomenon first observed over 45 years earlier by H. Kammerlingh Onnes. A superconductor is a metal which when cooled below its critical transition temperature, T_c, exhibits zero electrical resistance and the Meissner effect, the expelling of magnetic flux from the bulk of the sample. The BCS theory describes this transition as a condensation of electrons in the metal into a macroscopic quantum state. The electrons form weakly bound "Cooper pairs" of equal and opposite momenta. Cooper showed [2] that a Fermi sea is unstable against the formation of at least one bound pair in the presence of a weak attractive

potential. This result led BCS to propose a ground state of the form

$$|\psi_g\rangle = \prod_k (u_k + v_k\, c^*_{k\uparrow}\, c^*_{-k\downarrow})\ |\phi_0\rangle. \tag{2.1}$$

Here $c^*_{k\uparrow}$ is a creation operator that creates an electron of momentum $\vec{k}$ and spin up, $|\phi_0\rangle$ is the vacuum state with no particles, $|v_k|^2$ is the probability that the pair state $(\vec{k}_\uparrow, -\vec{k}_\downarrow)$ is occupied, and $|u_k|^2 = 1 - |v_k|^2$. These creation operators are a compact notational way of expressing the necessary antisymmetrization of the electron wavefunctions. We can see that the two creation operators specify the creation of a Cooper pair.

To calculate the coefficients u_k and v_k, a variational procedure was used; the pairing hamiltonian

$$H = \sum_{k\sigma} \epsilon_k n_{k\sigma} + \sum_{kl} V_{kl} c^*_{k\uparrow} c^*_{-k\downarrow} c_{-l\downarrow} c_{l\uparrow}, \tag{2.2}$$

where ϵ_k is the energy of the state $\vec{k}$ and $n_{k\sigma}$ is the occupancy, is minimized by taking

$$\delta\langle\psi_g|H|\psi_g\rangle = 0. \tag{2.3}$$

Furthermore they picked the attractive pairing potential, V_{kl}, to be a constant V up to some cutoff $\hbar\omega_c$ and zero at higher energies. When solved, this yields an equation for the energy gap Δ and solutions for u_k and v_k. The solutions for the occupation probabilities are given by

$$u_k^2 = \frac{1}{2}\left(1 + \frac{\xi_k}{E_k}\right)$$

$$v_k^2 = \frac{1}{2}\left(1 - \frac{\xi_k}{E_k}\right). \qquad (2.4)$$

In these equations ξ_k is the single particle kinetic energy referenced to Fermi energy, $\epsilon_k - \mu$, and E_k is the quasiparticle excitation energy, $(\Delta^2 + \xi^2)^{\frac{1}{2}}$. Several things can be inferred at this point. The first is that the energy gap Δ is the condensation energy of a pair, or similarly, it is the energy required to break a pair into two quasiparticles. Also our preliminary identification of Δ as an energy gap is justified because it is the minimum excitation energy.

An alternative formulation of the problem by canonical transformation was suggested by Bogoliubov [3]. Instead of using creation and annihilation operators for electrons, quasiparticle creation and annihilation operators are defined as linear combinations of the electron operators and the u_k and v_k. Using this transformation and some simplifying approximations, u_k and v_k can be found without using a variational technique.

There is a conceptual advantage to the Bogoliubov transformation approach. Because the probability factor u_k and v_k are fractional, a given electron state with definite $\vec{k}$ is partially full and partially empty. While this state stresses the many-body nature of the problem, it can be a hindrance to understanding. Because of the way that the transform is constructed, a quasiparticle state corresponding to $\vec{k}$ is either occupied or not. So while the quasiparticles have some features unlike normal holes or electrons, in many instances we can forget the differences and think of the excitations as we would in a semiconductor.

This facilitates a better physical understanding of processes like tunneling, which to first order, can be treated as it is in a normal metal or semiconductor.

Extending BCS theory to finite temperatures, it is possible to calculate the temperature dependence of the gap. Near T_c, it is found

$$\frac{\Delta(T)}{\Delta(0)} = 1.74 \left(1 - \frac{T}{T_c} \right)^{1/2}. \tag{2.5}$$

Far from T_c, the gap is essentially constant at its zero temperature value. From this and Eq. (2.4) we can infer qualitatively that the number of superconducting pairs, n_s, is large except near T_c, and that the number of quasiparticles is small. At zero temperature, all of the electrons are paired. It is also possible to predict $\Delta(0)$ given T_c. The BCS result is

$$2\Delta(0) = 3.528\ k_B\ T_c. \tag{2.6}$$

In practice, values of 2Δ are found ranging from 3.0 to 5.0 in conventional superconductors.

2.2 Ginzburg-Landau Theory

A macroscopic phenomenological theory of superconductivity was given by Ginzburg and Landau in 1950. Although largely ignored at the time, this theory has been shown to be an excellent supplement to the BCS theory. Several excellent reviews are available [4,5]. G-L theory has shown its real strength in dealing with applied fields, and with situations where Δ varies spatially, such as at interfaces. The theory begins with a pseudo-wavefunction order parameter $\psi = |\psi| e^{i\theta}$, where $|\psi|^2$

is a measure of the density of superconducting electrons and the phase θ is related to the superfluid velocity v_s. The theory was developed by writing the free energy of the superconductor in powers of $|\psi|^2$ and $|\nabla\psi|^2$, and minimizing using a variational technique. Gor'kov showed that the order parameter ψ is proportional to the BCS energy gap Δ. This theory is expected to be valid only near T_c, although it often gives good results for a larger temperature range. Another constraint on ψ is that it is small and has a slow spatial variation.

The spatial variation of ψ is at the heart of the theory. This theory has a characteristic length $\xi(T)$ which is called the Ginzburg-Landau coherence length. It is a measure of how rapidly ψ can vary without undue energy cost, and the decay length of the supercurrent at a boundary. At low temperatures and in pure materials, $\xi(T)$ reduces to the Pippard coherence length ξ_0 which is the minimum size of a Cooper pair. In dirty superconductors at low temperatures, $\xi(T)$ is the geometric mean of the Pippard length and the mean free path ℓ. Another important length is the magnetic penetration depth λ. Magnetic fields are screened from the interior of the superconductor by supercurrent and the fields decay at the surface with length λ. Similarly, supercurrent only flows in the outermost region of the conductor, where the fields are not screened.

One of the most important results to come out of G-L theory is the prediction of type II superconductivity. In certain superconductors with large λ and small ξ, it becomes energetically advantageous for the field to penetrate the samples. The field penetrates in a vortex, which is a region of the superconductor where ψ falls to zero and is now "normal". The radius of the vortex is ξ and the field penetrates over a larger

volume of radius λ. The ratio $\kappa = \lambda/\xi$ determines if a superconductor is type I or type II. Abrikosov calculated the exact break-over point as $\kappa = 1/\sqrt{2}$. The size of the field at which vortices first appear is called H_{c1}, and the field that drives the entire superconductor normal is H_{c2}. In the region between the two critical fields, the sample is said to be in the intermediate state.

In general, type II superconductors are more technologically useful. Materials with high T_c's, large critical current densities, and large critical fields are type II superconductors. There is a problem with type II superconductors however. In the intermediate state, the vortices are subject to the Lorentz force from the flowing supercurrent. This leads to a small dissipation. In many materials, this dissipation can be overcome by pinning the vortices. Typically, impurities or crystal defects can pin the impurities sufficiently that the superconductor shows no dissipation. However, thermal activation of the vortices can overcome the pinning leading to a phenomenon known as flux creep. At present, this effect is an important problem in the implementation of the new high-T_c ceramic superconductors.

G-L theory shows that supercurrent is linear in both the gradient of the order parameter and the vector potential $\vec{A}$. The superfluid momentum is given by

$$m\vec{v} = \hbar\vec{\nabla}\theta + 2e\vec{A}. \tag{2.7}$$

This result can be used to demonstrate one of the most startling results of superconductivity, magnetic flux quantization. For a wire of radius $r >> \lambda$, there is no supercurrent at the center of the wire, and the left

hand side of Eq. (2.7) is zero. If we consider a ring of this wire, then periodic boundary conditions force $\psi = |\psi|e^{i\theta}$ to be single valued, or θ to be itself modulo 2π. Integrating around the ring we find

$$2\pi n = -\oint \vec{\nabla}\theta \cdot d\vec{l} = \frac{2e}{\hbar} \oint \vec{A} \cdot d\vec{l} = \frac{2e\Phi}{\hbar}, \tag{2.8}$$

or $\Phi = n\Phi_0$, where $\Phi_0 = h/2e = 2.07 \times 10^{-7}$ gauss-cm^2. The flux inside the ring is quantized in units of Φ_0, the superconductor flux quantum. In situations where the flux threading the loop is not an integer number of flux quanta, circulating currents in the ring provide the necessary flux.

2.3 Weak Links and Junctions

When two superconductors are brought into close physical proximity, it is possible for current to tunnel between the two (Figure 2.1). At temperatures much less than T_c, there are very few thermally excited quasiparticles, and as a result a very small tunneling current. When the applied voltage exceeds $(\Delta_L + \Delta_R)/e$, the electron-like states of one the superconductors is aligned with the hole-like states of the other, so that current can flow. In an ideal junction at zero temperatures, there should be no current below the gap and a discontinuous rise in current at $(\Delta_L + \Delta_R)/e$, because the density of states is infinite at the gap edge. Thermal rounding and other imperfections prevent this.

Until 1962, it was believed that the probability for pair tunneling across a barrier was exceedingly small because it was a two particle tunneling process. That year, Josephson [6] showed that for a sufficiently thin tunneling barrier, phase coherence of the order

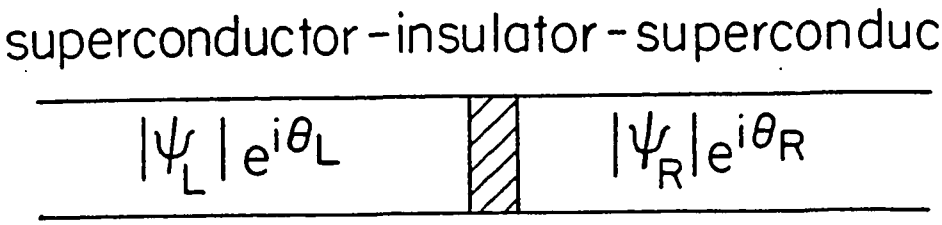

(a)

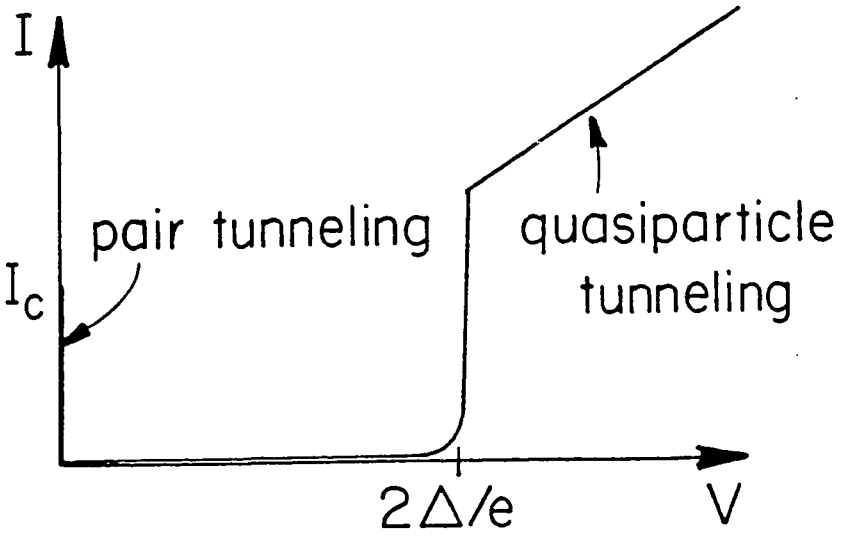

(b)

Figure 2.1 - (a) Superconductor-insulator-superconductor sandwich. (b) Current voltage characteristic for identical superconductors.

parameters of the two superconductors will cause pair tunneling to proceed with the same probability as single particle tunneling. He found that the current-phase relation for insulator tunneling to be

$$I_s = I_c \sin \theta, \tag{2.9}$$

where I_c is the maximum supercurrent, and $\theta = \theta_L - \theta_R$ is the phase difference of the order parameters on either side of the junction. In an ideal junction of identical superconductors, I_c should be $\pi/4$ times the current at the $2\Delta/e$ rise [7]. Josephson also found the voltage across the junction is related to the time derivative of the phase drop across the junction by

$$V = \left(\frac{\hbar}{2e}\right) \dot{\theta}. \tag{2.10}$$

This formula is also known as the a.c. Josephson effect and is the basis of the very precise measurements of $\hbar/e$ that have been performed using Josephson junctions.

While Eq. (2.9) applies only to SIS (superconductor-insulator-superconductor) structures with thin insulators, similar current-phase relationships exist for all sorts of weak link structure. Weak links can be formed by using semiconductor or normal metal (SNS) barriers, by a point contact between two superconductors, or by making small constrictions in the cross section of a superconductor (microbridges). Microbridges are typically made in thin films of superconductors by patterning a short constriction smaller than the G-L coherence length, ξ. This small area weakens the phase coherence across the two sides of the

bridge. In the non-SIS cases, the current-phase relationship is more complex than Eq. (2.9). It has the general form

$$I_s = I_c F(\theta), \tag{2.11}$$

where $F(\theta)$ is periodic and odd in the phase [8]. There is also a predicted term that is even in phase due to interference between the pairs and the quasiparticles. There is still some unresolved controversy surrounding this term, and in most applications, it can safely be ignored. The exact form for $F(\theta)$ and size of I_c depend strongly on the exact nature of the weak link. The materials, and geometric structure, of the weak link as well as the temperature and applied fields can interact strongly in determining the functional form of $F(\theta)$.

From a practical point of view there are great differences in the various types of junctions. Typically the barrier thickness of SIS junctions is 1 - 5 nm. These dimensions are beyond the reach of standard micro-fabrication techniques, so that these devices must be made in a sandwich geometry where the two superconducting electrodes are thin films grown in a stack with a thin native oxide grown between them. The situation is very different for SNS junctions. If the interface between the superconductor and the normal metal is clean enough, the superconducting order parameter extends into the normal metal for some distance. This effect is known as the proximity effect. The order parameter decays at some length characteristic to the normal metal known as ξ_N, the normal metal coherence length. This length can be very long ($\simeq 1\ \mu m$) in metals such as gold or copper. As a result, SNS junctions can be made in either stacked or planar geometries. Microbridges require

a constriction with dimensions comparable to the G-L coherence length. In materials such as tin or aluminum with large coherence lengths ($\simeq$ 1 μm), this is easy to fabricate. In other materials like niobium ($\xi \simeq 50$ nm) or $YBa_2Cu_3O_{7-x}$ ($\xi \simeq 1$ nm), this is nearly impossible.

A model for Josephson circuit elements that successfully predicts the dynamics for a junction was proposed by McCumber [9] and Stewart [10]. In this theory, they model the junction as a parallel combination of an ideal Josephson element, and intrinsic junction capacitance C, and a resistance R. This model is called the RSJ (resistively shunted junction) model, and is most applicable when an external shunt resistor is added to the junctions so that the quasiparticle resistance can be ignored. If the equations of motion for the RSJ are written down, it becomes clear that a mechanical analogy exits for the RSJ. It is a particle of mass C, moving through a viscous medium on a "washboard". In this analogy, the bias current is the overall tip of the washboard, the critical current is related to the sinusoidal modulation depth of the washboard, and the voltage is the speed of the particle.

For many applications, the extreme nonlinearity of the quasiparticle resistance is undesirable. Also, the I-V characteristic of a SIS junction is inherently hysteretic. In cases where these properties are undesirable, they can be eliminated by the addition of a resistive shunt where the resistance is chosen by the condition

$$\beta_c = \frac{2\pi I_c R^2 C}{\Phi_0} < 1. \tag{2.12}$$

The I-V characteristics for shunted and unshunted junctions are shown in Figure 2.2.

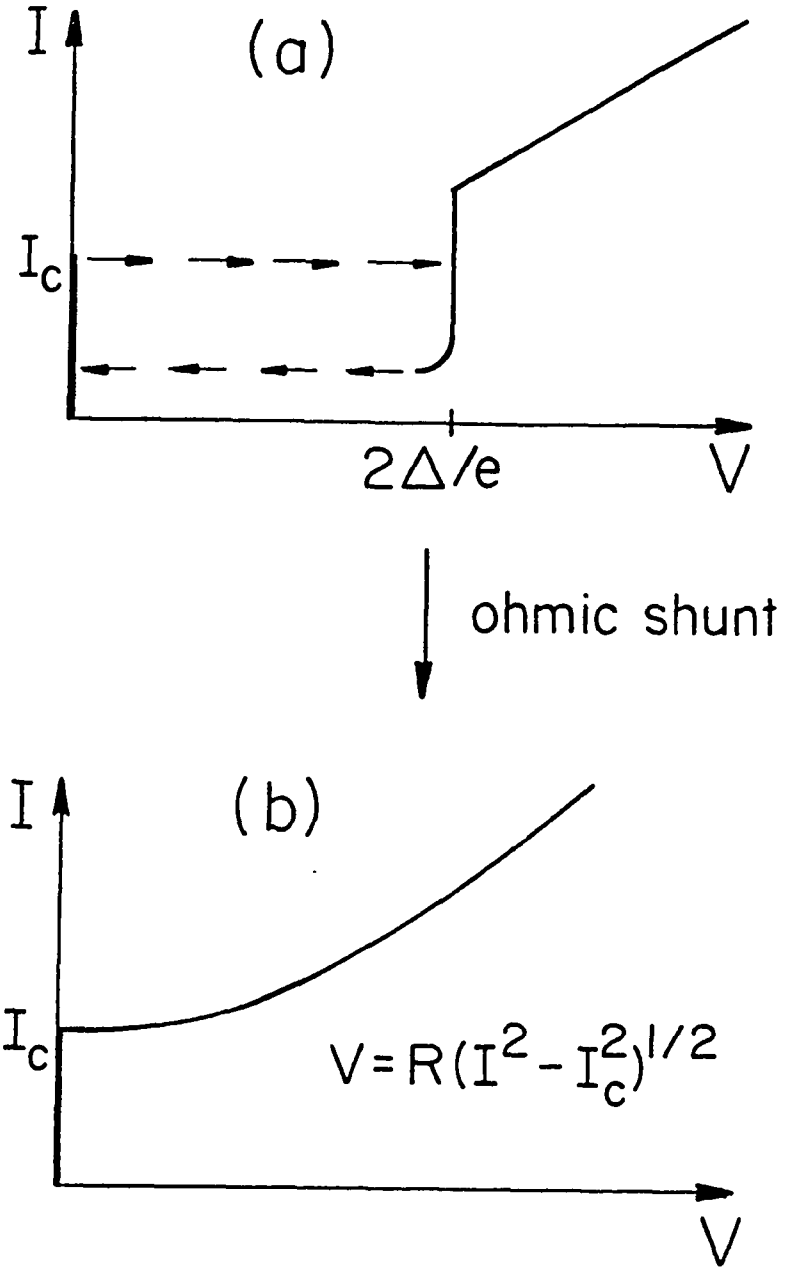

Figure 2.2 - Current-voltage characteristics for (a) unshunted junction and (b) shunted junction with $\beta_c < 1$.

2.4 SQUIDs

One of the most important applications of superconductivity to date has been the dc SQUID (Superconducting QUantum Interference Device). It is made by putting two weak link in parallel to form a closed superconducting loop. Such a device shows both critical current and voltage modulation in an applied magnetic field. As such it is the most sensitive detectors of magnetic flux known. It can also be used as a high sensitivity sensor for voltage and current when the appropriate external circuit elements are added.

The basic behavior of a dc SQUID is easiest to understand in terms of fluxoid conservation. As in Eq. (2.8) there is phase coherence around the loop of the SQUID. Here, we must take into account the phase drops at the weak links, and the circulating current in the loop. The important currents and phases are shown in Figure 2.3. The phase constraint for the d.c. SQUID is given by

$$2\pi n = \theta_1 - \theta_2 - \frac{2\pi(\Phi_a + LJ)}{\Phi_0}. \tag{2.13}$$

Here L is the loop self-inductance, J is the circulating current, and Φ_a is the applied flux. The net result (assuming identical junctions) is that at an integer number of applied flux quanta, there is no circulating current and the critical current of the SQUID is twice the individual junction critical currents ($2I_c$). At any other applied field, some circulating current must flow, and the overall critical current of the device is reduced to some value less than I_c. The amount of this reduction, or modulation depth is controlled by $\beta = 2LI_c/\Phi_0$. For a small β the modulation is deep, and for a large β, it is shallow.

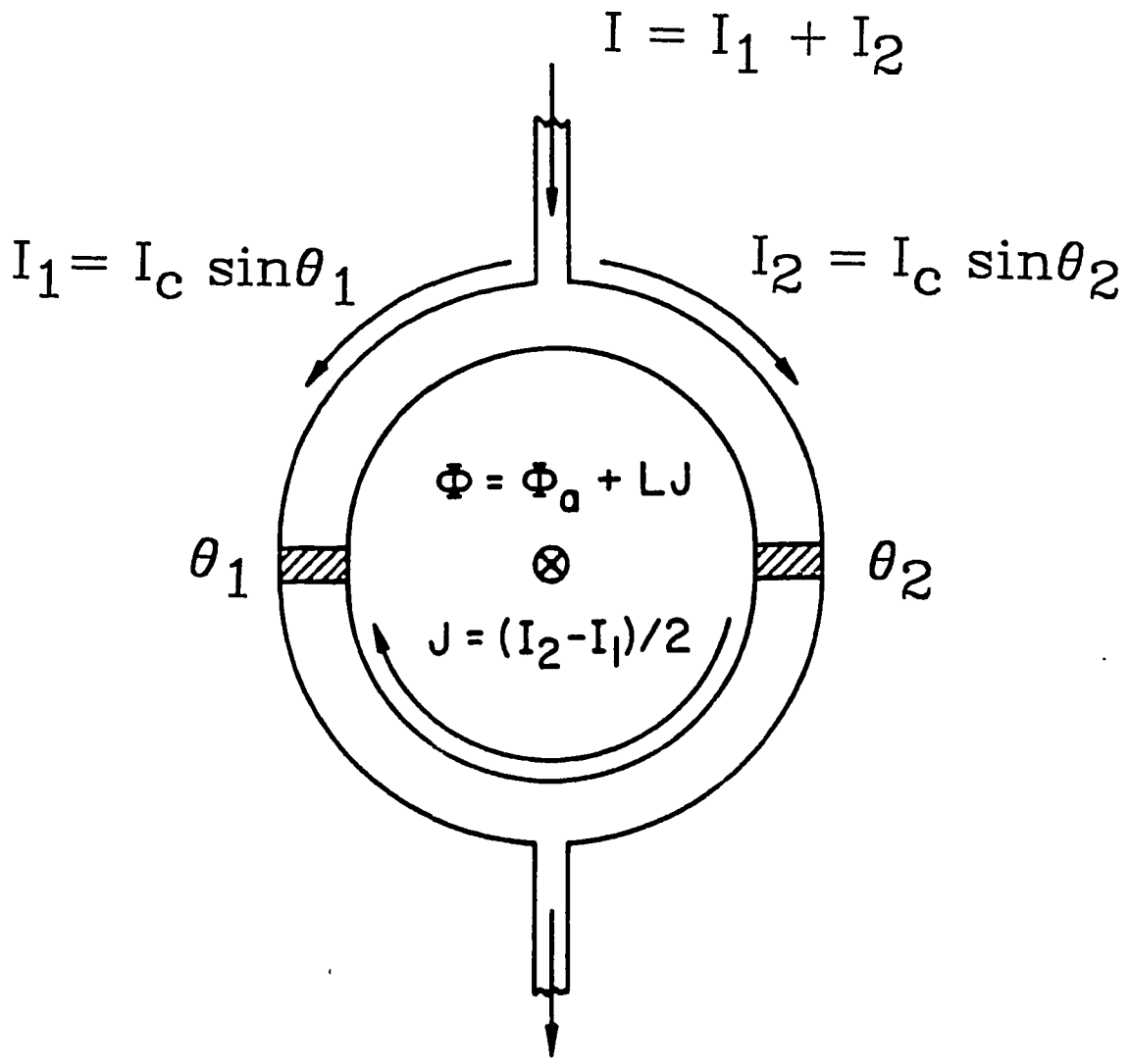

Figure 2.3 - Important currents and phases in the d.c. SQUID.

The dynamics of the dc SQUID are complex, and are usually solved by incorporating the RSJ model and using computer simulations. Despite this complexity, to first order, the SQUID behaves like an RSJ with a critical current that is a periodic function of applied flux. Figure 2.4a shows the modulation of I_c with flux and the corresponding modulation of the I-V characteristic. In practice, the SQUID is biased at constant current and the voltage is the output signal. Figure 2.4b shows the V-I characteristic and the corresponding modulation of voltage with applied flux. The bias point is picked so that the transfer function, $\partial V/\partial \Phi$ is maximized. In this mode of operation, the SQUID is a very sensitive flux to voltage converter with a small dynamic range (one flux quanta). To increase the dynamic range, the SQUID is usually operated in a flux locked mode, where a bias flux is applied to the SQUID. A feedback circuit is then employed to keep the SQUID at a fixed operating point. The signal flux is then equal and opposite to the feedback flux.

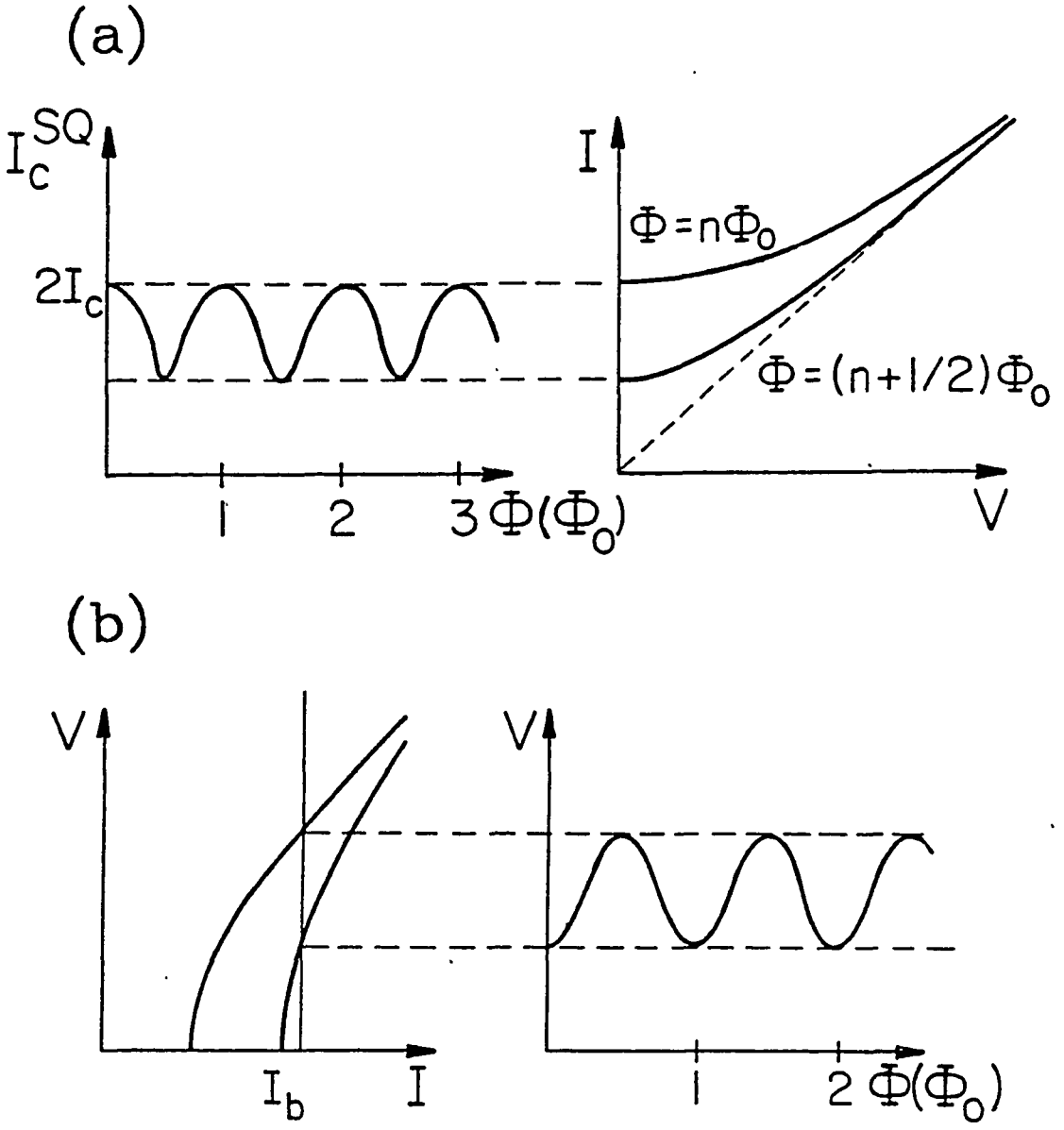

Figure 2.4 - (a) Modulation of I_c with applied flux, and corresponding modulation of I-V characteristic. (b) V-I characteristic and corresponding modulation of signal voltage with applied flux.

Chapter 3

NON-EQUILIBRIUM EXCITATIONS IN SUPERCONDUCTING ALUMINUM

In this chapter, we present results of an experiment involving non-equilibrium excitations in superconducting aluminum. Specifically we make measurements of a predicted, yet unmeasured excitation generation mode. This is the generation of a charge imbalance by the interaction of an electric field with a supercurrent.

3.1 Theory

In thermal equilibrium, the distribution of quasiparticles in a superconductor is given by the Fermi function f_k^0. If the sample is driven out of thermal equilibrium, the distribution of quasiparticles is now given by $f_k = f_k^0 + g_k$, where g_k is the non-equilibrium part of the distribution, and is a small perturbation near the Fermi surface. If we consider a one dimensional model, we can see four symmetry classes for g_k that correspond to deviations from equilibrium that are even or odd in $\vec{k}$ and $(\vec{k} - \vec{k}_F)$. These deviations correspond to the four non-equilibrium excitation modes in superconductors. The excitations that are odd about $(\vec{k} = 0)$, are well known excitations that arise in normal metals, and are manifested by electric current and heat current. The electric current $\vec{J}_n$ is an excess of holes moving one way, and electrons moving the other. This excitation is odd about both $(\vec{k} = 0)$ and $(\vec{k} = \vec{k}_F)$. An excitation that is odd about $(\vec{k} = 0)$ and even about $(\vec{k} = \vec{k}_F)$ implies that

quasiparticles of both charges are moving in the same direction. This excitation is the normal heat current $\vec{U}_n$. The two remaining symmetry classes are both even in $\vec{k}$ and are hence scalar quantities depending only on $|\vec{k}|$. These excitations have no analog in normal metals and arise because there are two fluids in the superconductor, and they can exchange both charge and energy. A distribution that is even about ($\vec{k} = 0$) and ($\vec{k} = \vec{k}_F$) implies merely a surplus in the number of quasiparticles, Δn, which corresponds to a shift in the superconducting energy gap, $\delta\Delta$. The last symmetry class, even about ($\vec{k} = 0$) and odd about ($\vec{k} = \vec{k}_F$), is an excess of holes compared with electrons. This is the charge imbalance Q^*, and is an excess of charge in the normal fluid of the superconductor. Because the effect we are studying is a predicted but unobserved means of generating charge imbalance, in the following sections we will treat the relaxation, generation and detection of charge imbalance more closely.

It has been shown that one useful way of looking at non-equilibrium excitations is as hydrodynamic variables [11]. Schmid [12] has used this idea to treat many non-equilibrium processes in a generalized hydrodynamic equation. He proposes that

$$\begin{bmatrix} \vec{J}_n \\ \vec{U}_n \\ Q^* \\ \Delta N \end{bmatrix} = \begin{bmatrix} \sigma & -L_T & \alpha\vec{v}_s & \beta e\vec{v}_s/k_BT \\ L_TT & -\kappa & \gamma T\vec{v}_s/e & \delta\vec{v}_s \\ -\alpha eN(0)\vec{v}_s & \gamma N(0)\vec{v}_s & -\tau_{Q^*}/e & -\tau_n/k_BT \\ \beta eN(0)\vec{v}_s & -\delta N(0)k_B\vec{v}_s & \tau_n/e & \tau_\Delta/k_BT \end{bmatrix} \begin{bmatrix} \vec{E}_n \\ \vec{\nabla}T \\ \vec{\nabla}\cdot\vec{J}_n \\ \vec{\nabla}\cdot\vec{U}_n \end{bmatrix}. \quad (3.1)$$

These equations are an extension of the familiar Onsager relations for a normal metal, adding new forces and currents. The upper 2 × 2 sub-matrix

is the standard transport equations for normal metals. Here, σ, κ, and L_T, are the electrical conductivity, thermal conductivity, and the thermoelectric coeffiecient. The additional "forces" and "currents" are unique to superconductors, and are a manifestation of the two extra degrees of freedom in a superconductor caused by the two fluids exchanging charge and energy. The most interesting and novel feature of Eq. (3.1) is the off-diagonal 2 × 2 sub-matrices. These terms couple vector forces to scalar currents or scalar forces to vector currents. The superfluid velocity $\vec{v}_s$ changes the distribution of quasiparticles, by exciting the quasiparticles on the forward side of the Fermi surface ($\vec{k}\cdot\vec{v}_s > 0$) to a higher energy, so that the equilibrium distribution is no longer symmetric in $\vec{k}$. The only term of this type to be studied experimentally is $Q^* = \gamma N_0 \vec{v}_s \cdot \vec{\nabla} T$ [13], The diagonal terms, and the term $\vec{J}_n = - L_T \vec{\nabla} T$ have also been studied experimentally [12,14,15]. The other terms have not yet been studied. The term we are studying is $Q^* = -\alpha e N(0) \vec{v}_s \cdot \vec{E}_n$ which predicts the generation of a charge imbalance by the interaction of superfluid and an electric field.

The number density of charge in a superconductor is given [11] in BCS theory by

$$Q_{TOT} = \frac{2}{\Omega} \sum_k v_k^2 + \frac{2}{\Omega} \sum_k (u_k^2 - v_k^2) f_k, \tag{3.2}$$

where Ω is the volume of the superconductor and the factor of 2 accounts for the sum over spin. The u_k and v_k are the usual BCS factors given by

$$u_k^2 = \frac{1}{2}\left(1 + \frac{\xi_k}{E_k}\right)$$
$$v_k^2 = \frac{1}{2}\left(1 - \frac{\xi_k}{E_k}\right). \tag{3.3}$$

Here, ξ_k is the kinetic energy of a quasiparticle relative to the pairs, $\xi_k = \epsilon_k - \mu_s$, and $E_k = (\Delta^2 + \xi_k^2)^{\frac{1}{2}}$. The first term in Eq. (3.2) represents the charge of the pairs, while the second term represents the quasiparticle charge. If we define an effective quasiparticle charge, q_k as (ξ_k/E_k), we may then write the total quasiparticle charge as

$$Q^* = \frac{2}{\Omega}\sum_k q_k f_k. \tag{3.4}$$

This effective quasiparticle charge implies that the quasiparticles are neither electrons or holes. For $\vec{k} >> \vec{k}_F$, the quasiparticles are electron -like and $q_k \sim 1$. For $\vec{k} << \vec{k}_F$, the quasiparticles are hole-like with $q_k \sim -1$. For quasiparticles near the Fermi surface, the effective quasiparticle charge is near zero, and the quasiparticles are neither electron-like or hole-like.

In equilibrium, the electron-like and hole-like branches of the excitation spectrum are populated equally, so that Q^* is zero. In a non-equilibrium situation, f_k is no longer the Fermi function, and Q^* may no longer be zero. The number of pairs is reduced by an amount equivalent to the charge imbalance in order to maintain overall charge neutrality. This causes the chemical potential μ_s to be reduced by an amount $\delta\mu_s$. In this way, charge imbalance and the pair chemical potential are intimately related. The reduction in the number of pairs can be calculated as $2N(0)\delta\mu_s$, where $N(0)$ is the single spin-density of states at the Fermi energy. From this, we see

$$Q^* = -2N(0)\delta\mu_s = -2N(0)(\mu_s - \mu_0). \tag{3.5}$$

If charge imbalance is injected in a steady state manner, at a rate $\dot{Q}_i$, the rate at which the charge imbalance relaxes can be measured. We define the inverse of this rate as the charge imbalance relaxation time, $\tau_Q{}^*$. More explicity,

$$\tau_{Q^*}^{-1} = \frac{\dot{Q}_i^*}{Q^*}. \tag{3.6}$$

This relaxation rate has been calculated [11,16] in the limit of $T \sim T_c$, or $\Delta << k_B T$, as

$$(\tau_{Q^*})^{-1} = \left(\frac{\pi\Delta}{4k_B T}\right)\tau_E^{-1}. \tag{3.7}$$

Here τ_E is the inelastic scattering time. In the absence of pair-breaking mechanisms, only inelastic scatterings can relax a charge imbalance. We can understand Eq. (3.7) as implying that only a fraction $\Delta/k_B T$ of all inelastic scatterings can relax the charge imbalance. The reasons for this are outlined below.

There are four processes that will relax the charge imbalance. (1) An injected quasiparticle causing a charge imbalance will have and energy $E \sim k_B T$. This quasiparticle on the (say) $\vec{k} > \vec{k}_F$ branch can scatter to a new energy E' on the same branch, or on a different branch. If it scatters to the same branch, it must scatter to a much lower energy $\Delta < E' < 2\Delta$ (where q_k is nearly zero) to relax the charge imbalance. Thus only a fraction $\sim\Delta/k_B T$ of these scatterings can relax Q^*. (2) A branch-

crossing scattering can certainly relax Q^*, however the coherence factor [4] for this process is only large when $\Delta < E' < 2\Delta$, again limiting the fraction of this type of scatterings available to relax Q^* to $\sim\Delta/k_BT$. Recombination processes can also relax the charge imbalance. The quasiparticle can recombine with another quasiparticle with energy E' on the same branch or with one on a different branch, to form a Cooper pair. Similar arguments can be applied to these cases. (3) If the quasiparticle recombines with a high energy quasiparticle on the other branch, they will have similar but opposite values of q_k. This will not cause Q^* to be reduced. Instead, opposite branch recombination must occur with a low energy quasiparticle with $\Delta < E' < 2\Delta$ where q_k is near zero. Again only a fraction $\sim\Delta/k_BT$ of these types of recombination processes contributes to the relaxation of Q^*. (4) For the case of recombination on the same branch, the coherence factor is again the limiting aspect. The coherence factor governing this recombination is small unless $\Delta < E' < 2\Delta$. For all four processes that can relax Q^*, there is some mechanism limiting the fraction of scatterings or recombinations that can relax the charge imbalance to $\sim\Delta/k_BT$ of all possible scatterings or recombinations.

The above argument considers only inelastic scattering. Normally, elastic scattering will only scatter the injected quasiparticle around the Fermi surface without affecting the value of Q^*. In the presence of pair-breaking perturbations, this is no longer true and elastic scattering can reduce the charge imbalance. Such pair breaking mechanisms include a supercurrent, magnetic impurities, or gap anisotropy. A corrected version of Eq. (3.7) must be used [17,18]:

$$(\tau_{Q^*})^{-1} = \left(\frac{\pi\Delta}{4k_bT}\right)\left(\frac{2\Gamma}{\tau_E}\right)^{1/2}$$

$$\Gamma = \frac{1}{2\tau_E} + \frac{1}{\tau_s} + \frac{Dp^2}{2h^2} + \frac{\langle a^2\rangle}{2\tau_1}. \qquad (3.8)$$

Here, τ_s is the magnetic impurity scattering time, $Dp^2/2h^2$ is the elastic scattering rate due to supercurrent, and $\langle a^2\rangle/2\tau_1$ is the rate due to gap anisotropy.

As well as having a characteristic decay time, Q^* also has a characteristic decay length λ_{Q^*}. Transport of the normal current $\vec{J}_n$ out of the region of charge imbalance carries quasiparticles with it causing the charge imbalance to decay spatially. A simple random walk argument leads to

$$\lambda_{Q^*} = \left(\frac{\sigma\tau_{Q^*}}{2N(0)e^2}\right)^{1/2} = \left(\frac{v_F l \tau_{Q^*}}{3}\right)^{1/2} \qquad (3.9)$$

where σ is the normal state conductivity, v_F is the Fermi velocity, and ℓ is the electronic mean free path.

In our experiments, we create charge imbalance by injecting quasiparticles into the superconductor across a tunnel barrier. The rate of injection of charge imbalance for this process has been calculated [11] as

$$\dot{Q}^* = \frac{F^* I_i}{e\Omega} \qquad (3.10)$$

where I_i is the injection current, and F^* is a dimensionless parameter

describing the efficiency of injection. This F^* has also been calculated, and in the limits of injection voltage, $eV_i >> k_BT$ and $eV_i >> \Delta$ as

$$F^* = 1 - \frac{\pi\Delta}{|2eV_i|} \qquad (3.11)$$

Typically, the injection voltage is in the limits given, and F^* is of order one.

A NIS junction is used to detect charge imbalance. This normal metal junction acts as a probe of the chemical potential of the normal fluid, which is shifted with respect to the superfluid chemical potential by the charge imbalance. A voltage V_d must be applied across this junction to keep the current flow zero. This voltage is related to Q^* by [17]

$$V_d = \frac{Q^*}{2N(0)e\, g_{ns}(0)} \qquad (3.12)$$

In this equation, $g_{NS}(0) = G_{NS}(0)/G_{NN}$ is the zero voltage conductance normalized to conductance at T_c.

If we combine Eqs. (3.6), (3.10) and (3.12) and solve for τ_Q^*, we find

$$\tau_{Q^*} = \frac{F^* I_i}{2N(0)\Omega e^2 V_d g_{ns}(0)} \qquad (3.13)$$

This is the basis for the many "three film" experiments that have been done in the field of charge imbalance. In these experiments, a sandwich of three films is made. The bottom film is the superconducting injector

film, the middle film is the superconducting film under study, and the top film is a normal metal detector. In this configuration, it is possible to measure τ_Q^* by applying an injection current and measuring I_i/V_d, or R_Q^*. These experiments have been used by many authors to measure some of the corrections to the relationship between τ_Q^* and τ_E suggested by Eq. (3.8). [19,20,21]

3.2 Experimental Details

We have performed two types of experiments measuring various aspects of charge imbalance. In the first, we essentially repeat a simple three film experiment with a few small differences required by our sample geometry. We do this to confirm our understanding of the sample and for comparison to other work. In the second experiment we measure the term in Eq. (3.1) $Q^* = -\alpha eN(0)\vec{v}_s \cdot \vec{E}_n$. This term predicts the generation of a charge imbalance by the interaction of a supercurrent and a normal electric field in the sample.

Our experiment requires a more complex geometry than the three film experiments. This is because it is difficult to introduce an electric field into the bulk of a superconductor. Except for small regions of non-equilibrium at the sample edges, the electric field is shorted out by the pairs. We should first consider more carefully what is meant by an electric field in a superconductor. In the hydrodynamic transport equations (Eq. 3.1), the field given as the driving force is $\vec{E}_n$. This is the electric field that drives the quasiparticles, which consists of two parts, the regular electric field, and the gradient of the chemical potential. $\vec{E}_n$ is really the gradient of not just the electric potential,

but the electrochemical potential, $\mu_0 + eV$, so that

$$\vec{E}_n = -\frac{1}{e}\vec{\nabla}(\mu_0 - eV) = \vec{E} - \frac{1}{e}\vec{\nabla}\mu_0. \tag{3.14}$$

The regular electric field, $\vec{E}$, has an additional constraint placed on it. In a steady-state situation, the electrochemical potential of the pairs must be zero to prevent the supercurrent from accelerating. This constraint is expressed by

$$\vec{E} - \vec{\nabla}\mu_s/e = 0. \tag{3.15}$$

Combining Eqs. (3.5), (3.14), and (3.15) we find

$$\vec{E}_n = -\frac{1}{2eN(0)}\vec{\nabla}Q^*. \tag{3.16}$$

This equation tells us how to apply the field we need. It is created by a gradient of charge imbalance. This gradient is generated by the spatial decay of the charge imbalance. The term we are studying, $Q^* = -\alpha eN(0)\vec{v}_s \cdot \vec{E}_n$, transforms into a term proportional to the supercurrent times the gradient of charge imbalance. We will refer to this effect as $I\vec{\nabla}Q$.

The sample layout for this experiment is shown in Figure 3.1. It consists of a 200 μm wide strip of aluminum. This is the sample strip, in which the charge imbalance will be generated and measured. On top of this strip, both injectors and detectors are fabricated. The injectors are large area (200 μm $\times$ 200 μm) SIS junction. These junctions have a small gap in the center, allowing a detector junction to be placed on the

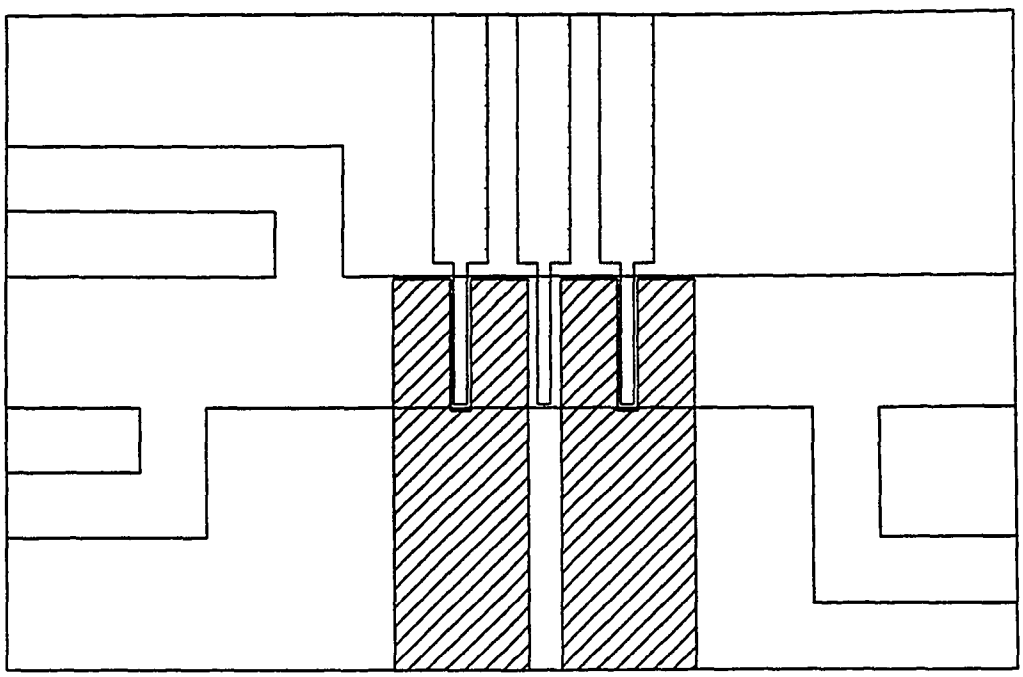

Al Sample strip

Al Injector

Cu Detector

Figure 3.1 - Sample configuration for the IVQ* experiment.

sample strip. This is shown more clearly in the side-view diagram of Figure 3.2(a). There are three NIS detector junctions. One at each injector, and one placed between the two detectors. Fabrication details for these junctions are presented later in this chapter.

The reasons for this geometry becomes clear when we consider how the sample is to be operated. There are two modes of operating this sample; symmetric injection, and asymmetric injection. The spatial distributions for Q^* and $\vec{\nabla}Q^*$ can be calculated for a given geometry if $\lambda_Q{}^*$ is known. Figure 3.2(b) shows calculations of Q^* and $\vec{\nabla}Q^*$ for symmetric injection. These calculations are for illustrative purposes only, and use a typical value of $\lambda_Q{}^*$ for aluminum in the temperature range studied. In this case, both injectors are biased at equal currents, causing $\vec{\nabla}Q^*$ to be zero in the region between the injectors. Asymmetric injection is shown in Figure 3.2(c). Here, the injectors are operated at equal but opposite currents, causing $\vec{\nabla}Q^*$ to be maximized in the region between injectors. This arrangement of injectors and detectors allows us to study the charge imbalance generated by $I\vec{\nabla}Q^*$ for different values of $\vec{\nabla}Q^*$, and enables us to verify the bi-linear nature of the effect. We are also able to repeat "three film" type experiments as a way of checking our understanding of the apparatus and sample.

3.2.1 Sample Fabrication

The samples were made by standard optical micro-lithographic and thin-film techniques. The masks used for patterning were written with an electron-beam lithography system developed by our group [22]. Patterning of the films was carried out using the lift-off process. In this process, a stencil of photoresist is made on the substrate, through

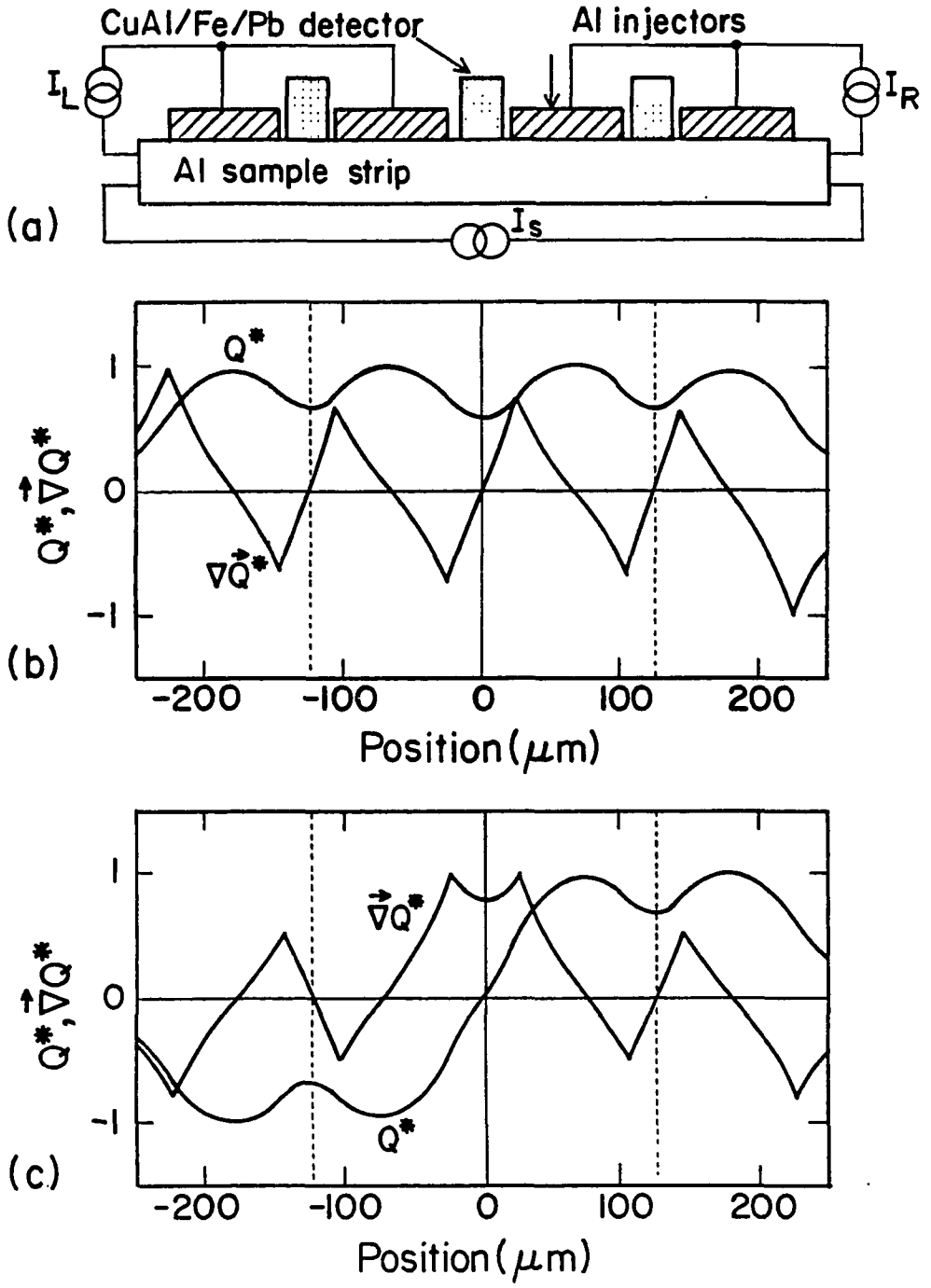

Figure 3.2 - (a) Side view of sample with currents and voltages shown. (b) Example calculations of Q^* and $\vec{\nabla}Q^*$ for symmetric injection. (c) Example calculations of Q^* and $\vec{\nabla}Q^*$ for asymmetric injection.

which the film is deposited. The stencil is then removed, lifting off any unwanted film. This process is explained in more detail in the next chapter. We used glass microscope slides cut into 1 cm × 2.5 cm pieces for substrates.

A niobium ground plane was the first film deposited. This film was deposited by dc magnetron sputtering. The purpose of the ground plane was to improve the cross-sectional uniformity of the supercurrent in the Al sample strip. The Nb was deposited to a thickness of 200 nm, and the top 50 nm was anodized in NH_4OH to form a Nb_2O_5 insulating layer. To insure that the ground plane was insulating, 100 nm of SiO and 10 nm of Ge were then thermally evaporated onto the entire substrate. We use germanium because it is highly mobile on the surface, and tends to fill in any pinholes in the insulating layers.

The sample was then prepared for the deposition of the aluminum sample strip. Photoresist was spun on, baked, exposed and developed leaving the lift-off stencil. The sample was then mounted in diffusion-pumped thermal evaporator. We pumped the system to its base pressure of 1×10^{-6} Torr. Before depositing the sample strip, we cleaned the sample by ion-milling at 500 V and 0.1 mA/cm^2 for 30 seconds. The aluminum was then evaporated from a resistance heated tungsten coil. To assure the cleanest possible Al, we deposited at a rate of at least 3 nm/s at the base pressure of the evaporator. The high rate assures large grain size with a minimum amount of impurities. We deposited the aluminum to a final thickness of 200 nm. After deposition, we removed the sample from the evaporator, and immersed it in acetone to remove the lift-off stencil.

The deposition of the injectors and detectors follow similar steps to the sample strip. The sample is patterned for lift-off and remounted in the evaporator. We then clean it with ion-milling and deposit the film. The difference in fabricating the injectors and detectors lies in the materials used, and that a tunneling barrier to the sample strip must be made. The injectors are made of aluminum to form an SIS junction, while the detectors are made of copper to form an NIS junction with the sample. The barriers required for the two junctions are quite different. The injectors are a very large area junction and require a moderately high resistance ($\simeq$10 Ω). This is because at a typical injection voltage ($\simeq$30 Δ/e), the injection current will be large enough to inject a sizable charge imbalance, but small enough not to cause significant heating. The detectors are an order of magnitude smaller than the injectors, but require a resistance three to four orders of magnitude smaller than the injectors. The resistance of the detectors must be that small (<10 mΩ) so that they will have the needed voltage sensitivity. The Johnson noise in a 10 mΩ resistor at 1.2 K is about 0.6 pVHz$^{-\frac{1}{2}}$. The expected signal size is picovolts (assuming α goes as τ_Q*), so we need this kind of sensitivity.

We found many difficulties in making reliable tunnel junctions on the Al sample strip. In much of the older "three films" type of experiments, the samples were made without breaking vacuum between the depositions. A mechanical aperture-mask changing apparatus was used to perform the patterning *in-situ*. This technique is not possible for the fine geometries that we require. As a result we needed to find ways to deal with the extremely tough native oxide that grows on Al when it has

been subjected to atmospheric conditions. The technique that was most reliable was the use of a protective overlayer on the sample strip. After the aluminum was deposited, it was lightly oxidized by exposing it to O_2 at 60 mTorr for 30 seconds. The evaporator was then pumped out again, and 10 nm of Cu was deposited over the Al. This yielded a structure that could be cleaned by ion-milling without much damage to the underlying Al. We made the tunneling barriers for the injectors by milling the sample at 500 V and 0.5 mA/cm^2 for 30 seconds and oxidizing in O_2 at 50 mTorr for 2 minutes. We then evaporated a 25 nm Ge barrier to get a high enough resistance, followed by 300nm of Al evaporated at 3 nms^{-1} to form the counter-electrode. We made the low resistance barriers for the detectors by ion milling the sample strip surface at 500 V and 0.5 mA/cm^2 for 30 seconds. The counter electrode was then deposited. First 350 nm of Cu (3 wt. % Al) was evaporated from a tungsten boat. The Cu is followed by 7.5 nm of Fe and 200 nm of Pb (10 wt. % In). The Pb/In, which is superconducting at the measurement temperatures, eliminated the series resistance of the detectors which would have produced large Johnson noise. Without the Fe, proximity effect coupling through the Cu causes the detector to be superconducting.

3.2.2 Measurement Techniques

To achieve good temperature uniformity in the sample, the sample was immersed in the pumped liquid helium bath. The sample was mounted on a phenolic block with a small amount of vacuum grease. A calibrated Ge thermometer (Lake Shore Cryogenics #19176) was mounted on a small copper block that was also immersed in the bath. Electrical connections to the sample were made by tinned #36 copper magnet wire, pressed onto the

sample with indium pads. These leads were then soldered onto a terminal block on the phenolic sample holder. Connections to room temperature were made with twisted pairs of #40 copper magnet wire. To eliminate noise pick-up in these long leads, they were terminated on both ends by 100 Ω metal film resistors.

For the sensitive charge imbalance measurements, we used a null-balancing rf superconducting quantum-interference device (SQUID) voltmeter. Figure 3.3 shows the operating configuration for a SQUID voltmeter. The SQUID is used to detect any current through the circuit, and negative feedback is used null currents caused by the voltage at the sample. The standard resistor (R_s) was a small length of 0.065" diameter copper wire. In the temperature range of interest, R_s had a value of 1.5 $\mu\Omega$, and because of the narrow temperature range studied, R_s was found to be temperature independent. The external resistor, R_e was then adjusted to be 15 kΩ, to give an overall system gain of 10^{10}. To make connections to the various injector and detectors with this voltmeter, a superconducting switch was built. This switch consists a small circuit board with eight heavily tinned copper fingers. These fingers are broken in the middle, and contact is made by a shorting bar. The shorting bar is a small piece of phenolic with tinned Cu-Be contact springs. The phenolic piece is attached to a thin wall stainless tube that exits the cryostat at the top through a quick-connect fitting. This enables us to change the switch positions. To test the switch, a superconducting loop is made (including the switch), and the SQUID is used to determine the R/L decay time of a current induced in the loop. The switch was found to work very well. Superconducting leads from the sample to the switch

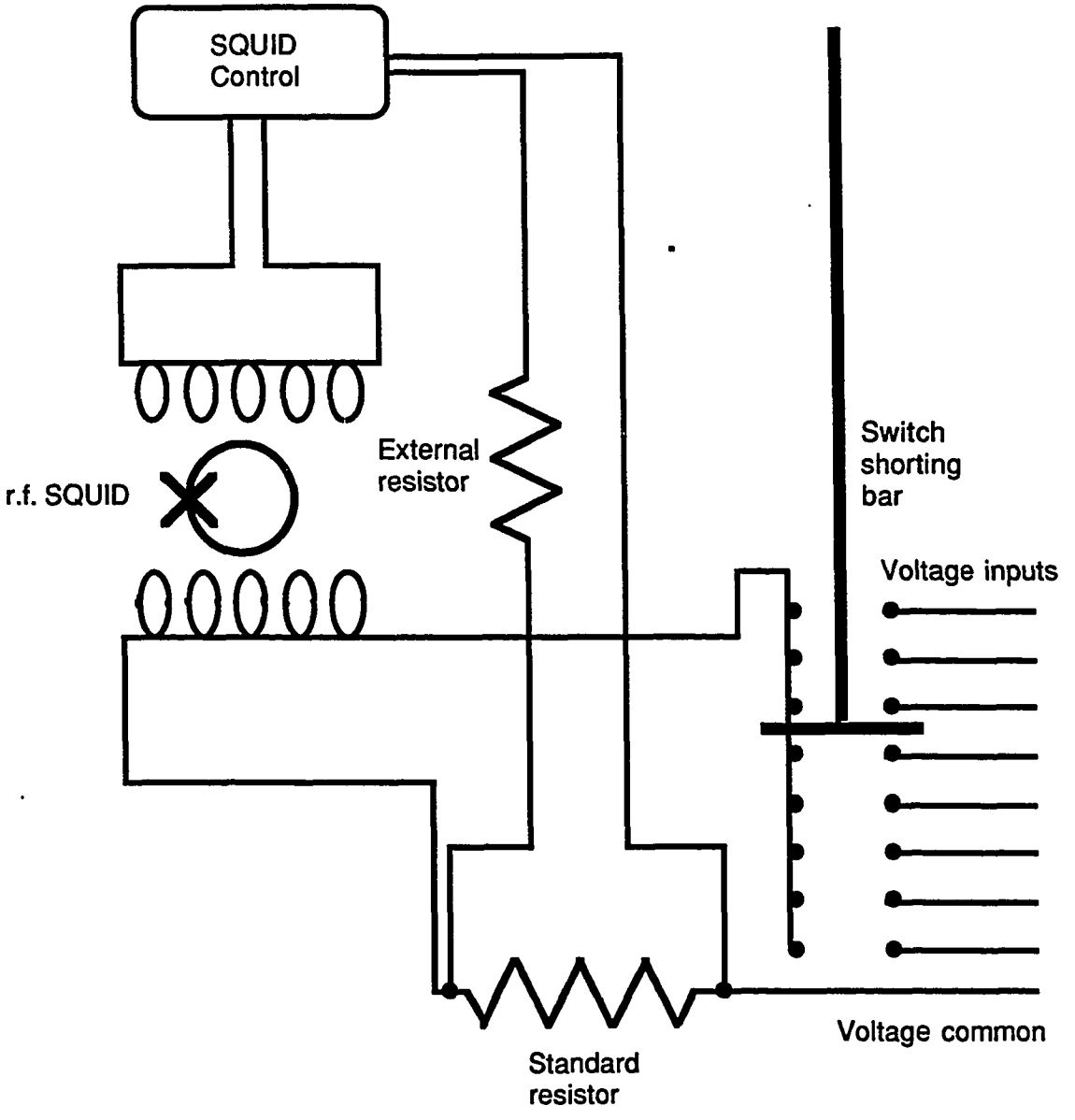

Figure 3.3 - Schematic diagram of null-balancing SQUID voltmeter including superconducting switch.

terminal block was made by tinned Cu-clad Nb-Ti wire which was pressed with indium pads onto the sample, and soldered on the terminal block.

Temperature control is critical in this experiment because of the strong temperature dependence of τ_Q^*. The entire range of measurement is between the lowest attainable temperature of 1.0 K, and the T_c of Al (about 1.2 K). For this reason the sample was immersed in the liquid helium bath. At these temperatures, helium is below the λ-point, and is a superfluid. As a result, thermal gradients and bubbles are virtually non-existent. To heat the bath, a non-inductively wound coil of manganin wire with a resistance of 50 Ω was used. Measurements of the thermometer resistance were made with a four-lead ac bridge. When regulating the system at a fixed temperature, the error signal from the bridge was used to drive a three-term control circuit that was connected to the heater. This thermometry system was found to stabilize quickly, and with care, it could achieve temperature stability of better than 1 mK over the desired range.

The entire sample and superconducting voltmeter circuit was enclosed in a lead shield, and the cryostat was surrounded by μ-metal shield. The cryostat is located in an rf shielded room. Ground loops and 60 Hz pick-up were minimized by using battery operated current supplies and preamplifiers. Also a specially constructed opto-isolated digital-to-analog converter was used to put the experiment under computer control. To minimize microphonic pick-up, all leads were mechanically secured, and the cryostat was connected to the pumping station through a balanced bellows arrangement.

3.3 Experimental Results

Before looking for the IVQ^* effect, we operated samples in the symmetric injection mode to measure τ_Q^* for comparison to previous work. The two most important results for comparison are the temperature dependence of τ_Q^* and the value of τ_E, the inelastic scattering time which is temperature independent, but highly material dependent. Near T_c, τ_Q^* has the same temperature dependence as $\Delta(T)^{-1}$. BCS theory gives this as $\Delta(T) \sim (1-T/T_c)^{\frac{1}{2}}$ [4]. Chi and Clarke [19] give a review of values of τ_E determined by different methods. Though τ_E is strongly material dependent, the value found in the cleanest films is about 11 ns. More recent work by Mamin, Clarke and Van Harlingen [15] points to some new difficulties. Their experiment measured the charge imbalance generated in aluminum thin films by a divergence of normal current near the end of a sample. The divergence of the current was caused by a temperature gradient. In performing this experiment they needed to make careful measurements of λ_Q^*. These were performed by using a series of exponentially spaced detectors. A charge imbalance is injected at one end of the probes, and the decay length was measured directly. When τ_E is calculated from the obtained value of λ_Q^*, an extremely small value of 2 ns is obtained. Mamin *et al.* were concerned with this result and fabricated "three films" samples concurrently with "length" samples. The "three film" samples gave values for τ_E in good agreement with other work. These results suggest that there is some excess scattering occuring, causing the suppression of the scattering lengths. Recent work [23] in niobium suggets that crystallographic effects can lead to

anomalous quasiparticle diffusion lengths, perhaps causing this observed difference between length measurements and three film measurements.

The procedure for taking data is the same as a three film experiment. The detector voltage is measured as a function of injected current at a variety of temperatures. Data can be taken using one of the two injectors and one of the three detectors. We took data for all configurations. Some examples of the raw data are shown in Figure 3.4.

Because of our geometry, our experiments are neither quite a length measurement nor a three film experiment. The split injectors with the detectors in the middle force a geometrical correction due to the decay of Q^* in the split detector region. This geometrical correction involves $\lambda_Q{}^*$, which is a function of $\tau_Q{}^*$. For the case of the center and either detector we have

$$Q^*_{det} = Q^*_0 \frac{\lambda_Q}{a} \sinh\left(\frac{a}{\lambda_Q}\right) e^{-b/\lambda_Q}, \tag{3.17}$$

where Q^*_{det} is the charge imbalance seen at the detector, Q^*_0 is the charge imbalance at the injector, a is the detector half width, and b is the distance from the center of the detector to the nearest edge of the injector. This factor ignores the far portion of the split injector, which is a good approximation given the expected size of $\lambda_Q{}^*$ for Al in the temperature range studied. To calculate $\tau_Q{}^*$ from $R_Q{}^*$ we need to modify Eq. (3.13). If we combine Eq. (3.9) and Eq. (3.13) and solve for all terms containing $\lambda_Q{}^*$ we get

$$H(\lambda) = \frac{\lambda^3}{a} \sinh\left(\frac{a}{\lambda}\right) e^{-b/\lambda} = \frac{\sigma\, \Omega\, g_{ns}(0)\, R_Q{}^*}{F^*}. \tag{3.18}$$

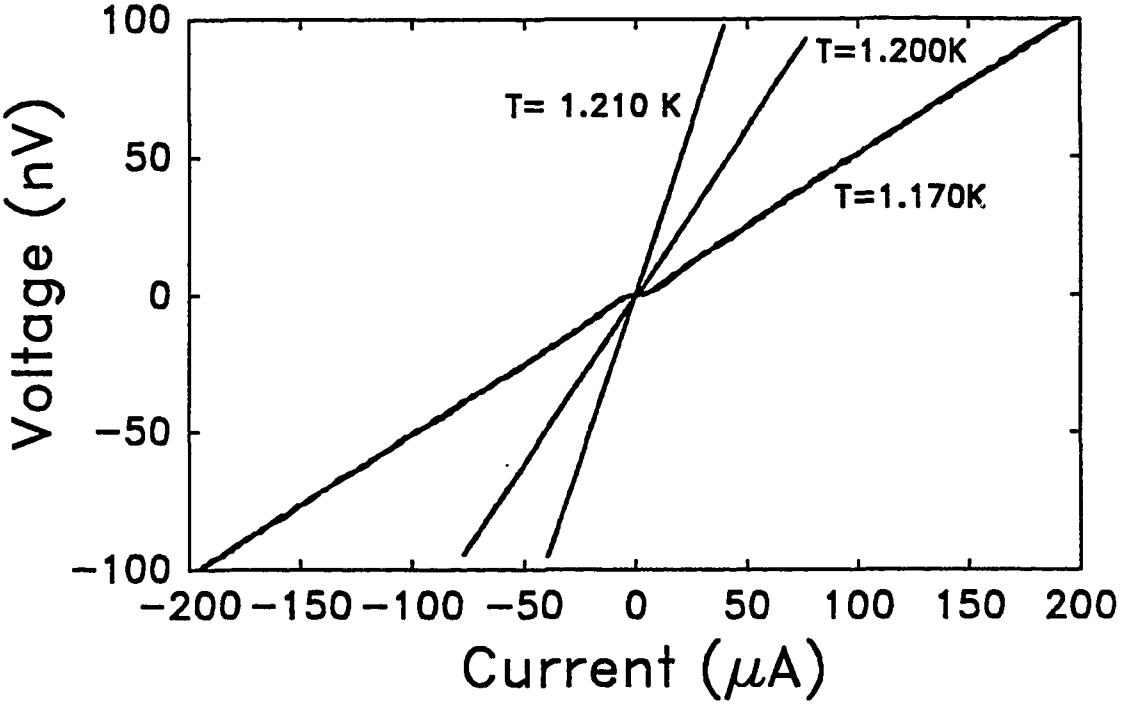

Figure 3.4 - Example data for symmetric injection. Detector voltage plotted against injection current at three temperatures.

The right hand side of this equation are all measurable or calculable quantities. The charge imbalance diffusion length is then calculated numerically from the function $H(\lambda)$, and τ_Q^* is calculated from λ_Q^*. The charge imbalance decay time τ_Q^*, and the inelastic scattering time τ_E are plotted *vs.* $(1-T/T_c)$ in Figure 3.5. We find that τ_Q^* has the predicted temperature dependence for temperatures near T_c. As the sample is cooled further, this relationship starts to break down as expected. The value of τ_E calculated from τ_Q^* is 7 ± 2 ns, and is independent of temperature near T_c. This value compares well with value obtained by Chi and Clarke [19] of 11 ± 2 ns, but is somewhat smaller. This difference could be explained if our films were dirtier than theirs, but by all conventional measurements (T_c, ρ(T=4.2 K), and resistance ratio), our films are as clean as theirs. The other possible explanation is that because we are observing at some distance from the injector, we are seeing some of the excess scattering the Mamin *et al.* [15] see in their length experiment.

We then operated the sample in the asymmetric mode in order to observe the $I\nabla Q^*$ effect. Here, currents of opposite polarities were applied to the two injectors. The size of these currents was adjusted so that no voltage was detected at the center detector. This insured that there was no charge imbalance at this detector. The injection currents, injection voltages, and detector voltages at each injector were measured. These measurements allow us to calculate ∇Q^* or $\vec{E}_n$. The voltage at the center detector was then measured as a function of applied supercurrent I_s. A plot of typical raw data for positive, negative, and zero values of ∇Q^* is shown in Figure 3.6. This plot shows the correct sign dependence of the expected effect, and also that with no gradient of

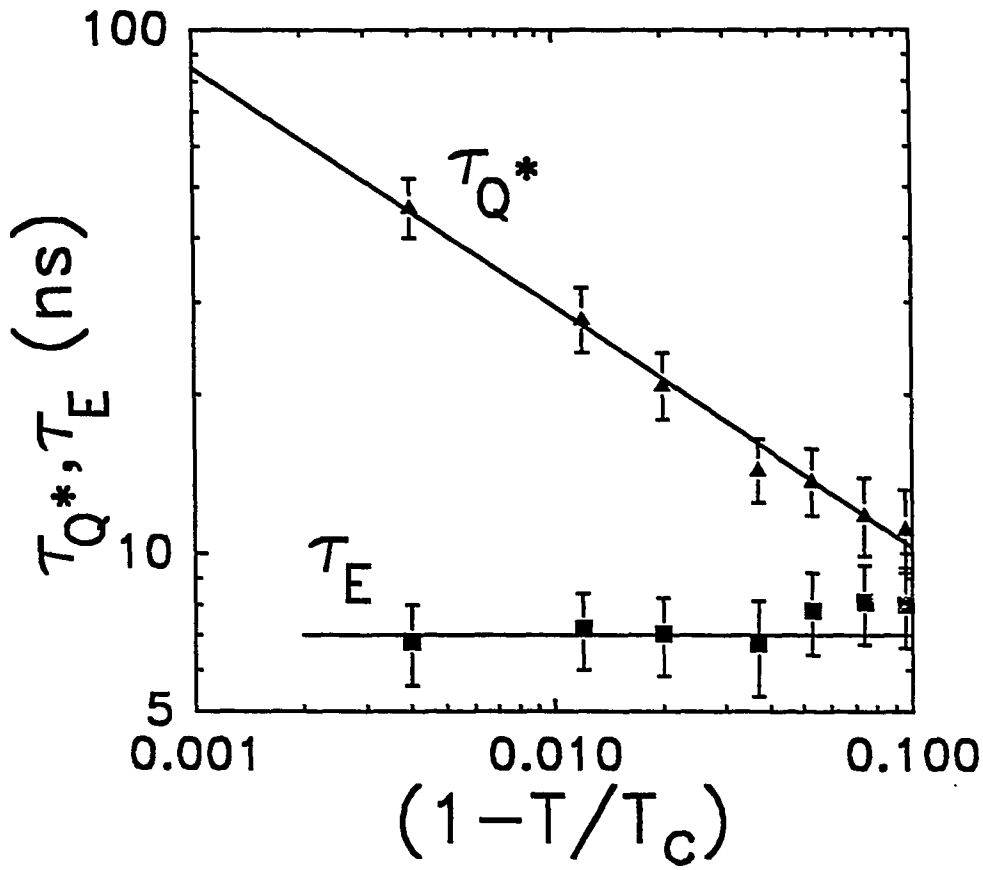

Figure 3.5 - Charge imbalance decay time, τ_{Q^*}, and inelastic scattering time, τ_E, plotted against $(1-T/T_c)$.

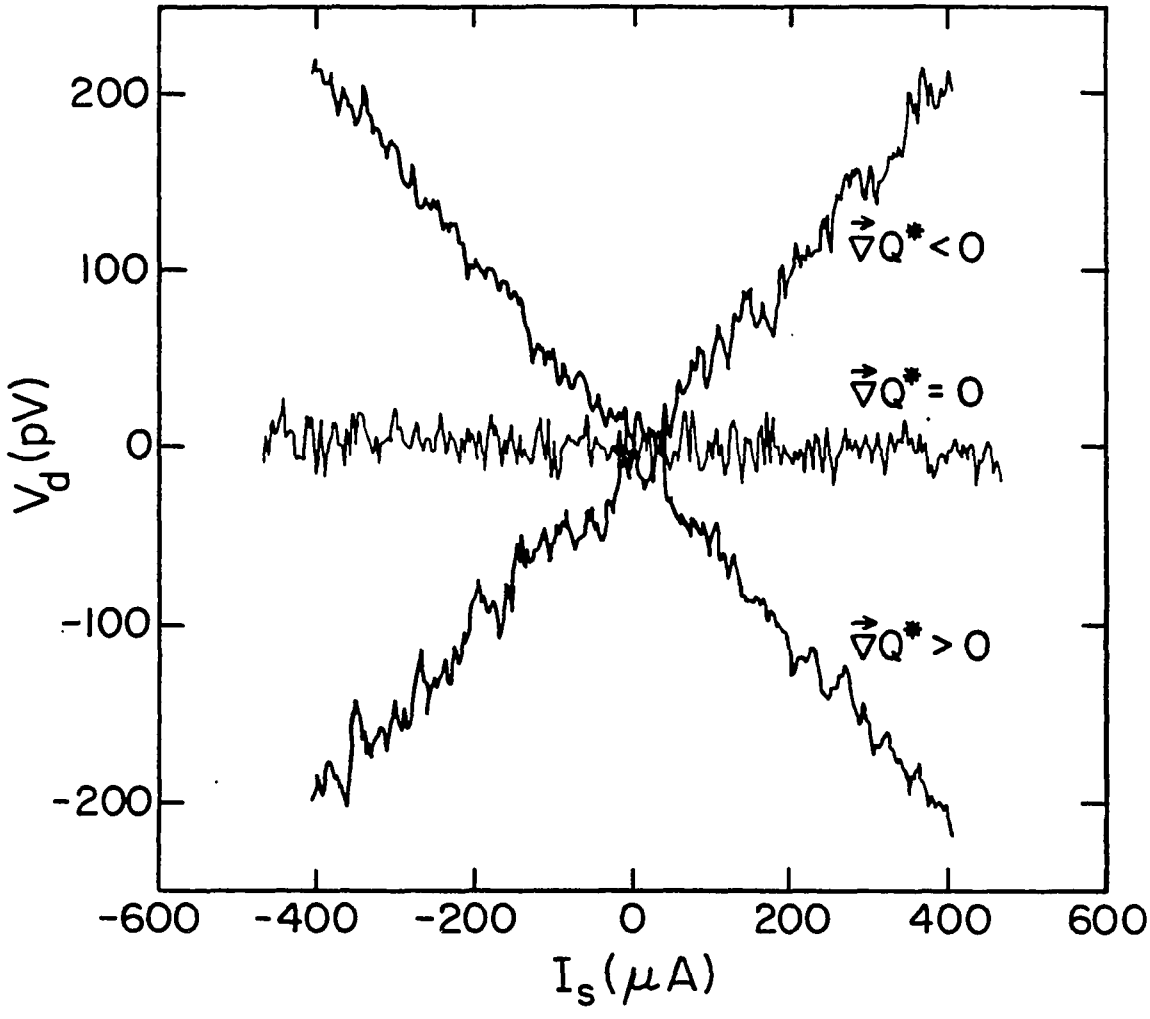

Figure 3.6 - Typical raw data for IVQ* experiment. Detector voltage plotted against supercurrent for three different injection configurations.

charge imbalance there is no charge imbalance generated by the supercurrent. Also demonstrated is the linearity of the observed effect with supercurrent.

Calculation of $\vec{E}_n$ from the two detector voltages V_R and V_L requires similar geometrical corrections to those needed to calculate τ_Q^*. Since the injector is split, the voltages measured at the side detectors are not an exact measure of Q^* at the injector. The corrected formula for electric field is

$$\vec{E}_n = (V_R - V_L) \frac{\sinh(A/\lambda)\ (e^{-B/\lambda} - e^{-C/\lambda})}{\lambda \sinh(a/\lambda)\ (e^{-b/\lambda} + e^{-c/\lambda})}. \tag{3.19}$$

In this equation, a is the side detector half width, b is the distance from the side detector to the near edge of the injector, c is the distance from the side detector to the far edge of the injector. The uppercase A, B, and C represent the same quantities for the center detector. The above equation assumes the detectors and injectors are symmetrically placed. This is reasonable given that typical lithographic inaccuracies of 1 or 2 μm are much smaller than λ_Q^* which is typically 50 μm in this experiment. The actual values for the geometric factors are measured from electron micrographs of the actual samples. Since the value of λ_Q^* is well characterized by the earlier τ_Q^* measurements, it is straightforward to calculate $\vec{E}_n$ from V_R and V_L.

To verify the linearity of the generated charge imbalance with $\vec{E}_n$, V_d/I_s is plotted against $\vec{E}_n$ in Figure 3.7. It is very surprising that all the data falls on the same line. We would expect to get a family of lines - one for each temperature. This lack of temperature dependence in

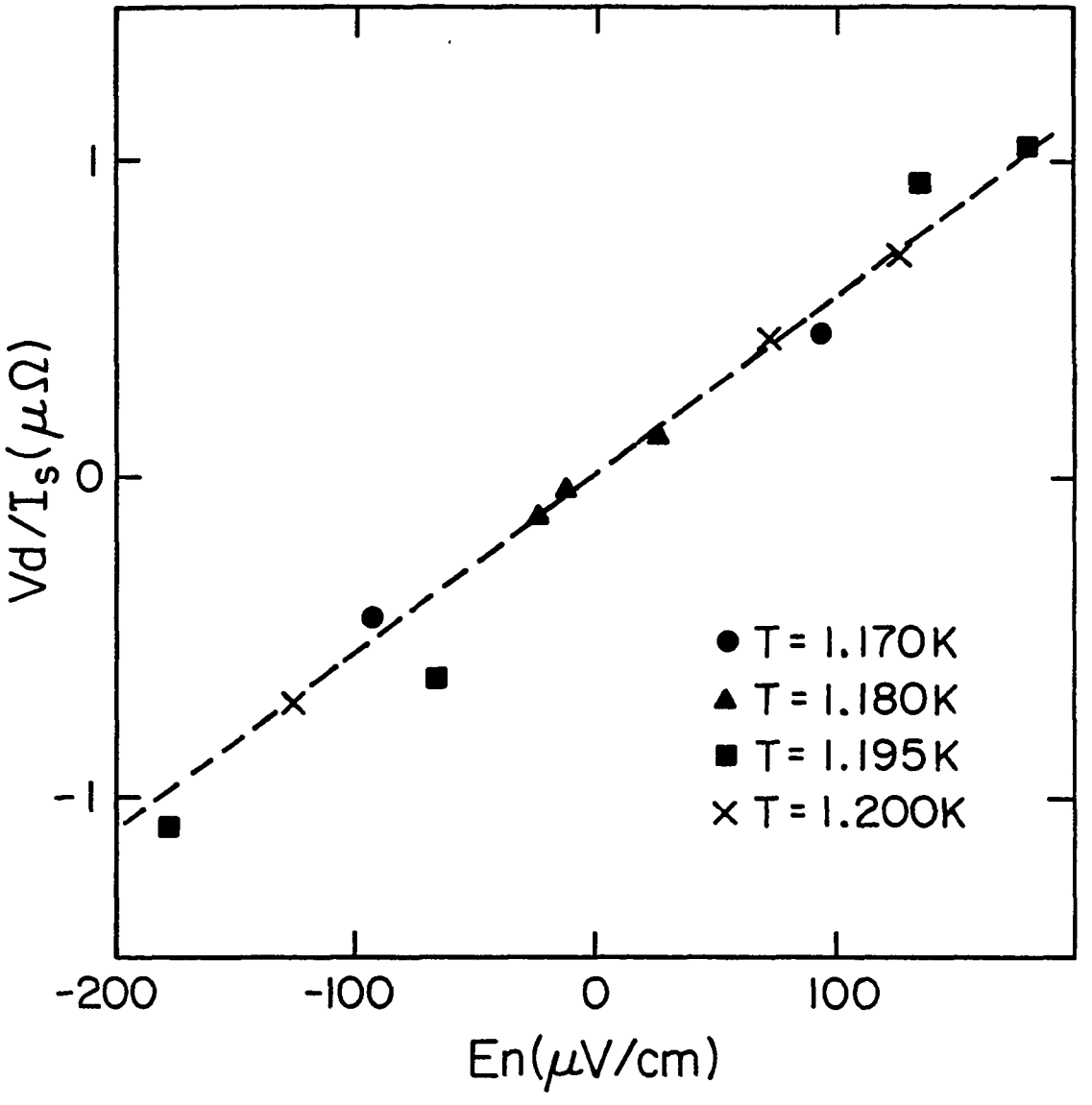

Figure 3.7 - Detector voltage normalized by supercurrent (V_d/I_s) plotted against $\vec{E}_n$ for various temperatures.

this figure does not imply that the coefficient for this effect in Eq. (3.1) is temperature independent. The term we are studying is $Q^* = -\alpha eN(0)\vec{v}_s\vec{E}_n$. The supercurrent I_s can be expressed as

$$I_s = \frac{e\ v_s\ n_s}{A}, \tag{3.20}$$

where n_s is the superfluid density, and A is the cross sectional area of the sample strip. We can combine Eqs. (3.1), (3.12), and (3.20) and solve for the slope of Figure 3.7,

$$\text{slope} = \frac{\alpha\ A}{2\ n_s\ g_{ns}(0)}\ . \tag{3.21}$$

It is not that α has no temperature dependence, but that the temperature dependence of α and n_s cancel, leading to a slope with no temperature dependence. This equation can also be used to calculate the value of α which is plotted against $(1-T/T_c)$ in Figure 3.8. Also plotted on this graph is τ_Q^*. Schmid [12] calculates that in the clean limit that α should be equal to τ_Q^*. From this we might expect that it should have the same temperature dependence as τ_Q^*, $(1-T/T_c)^{-\frac{1}{2}}$, not the observed temperature dependence of $(1-T/T_c)$.

The reasons for this great discrepancy in temperature dependence are unclear. In the temperature range studied, our samples are in the dirty limit, where the mean free path is much less that the coherence length. No calculations for α exist in the dirty limit. Calculations of the transport coefficients are difficult in the dirty limit where the large amount of elastic scattering is constantly rearranging the quasiparticle distribution. Also, as Eq. (3.8) shows, elastic scattering can relax

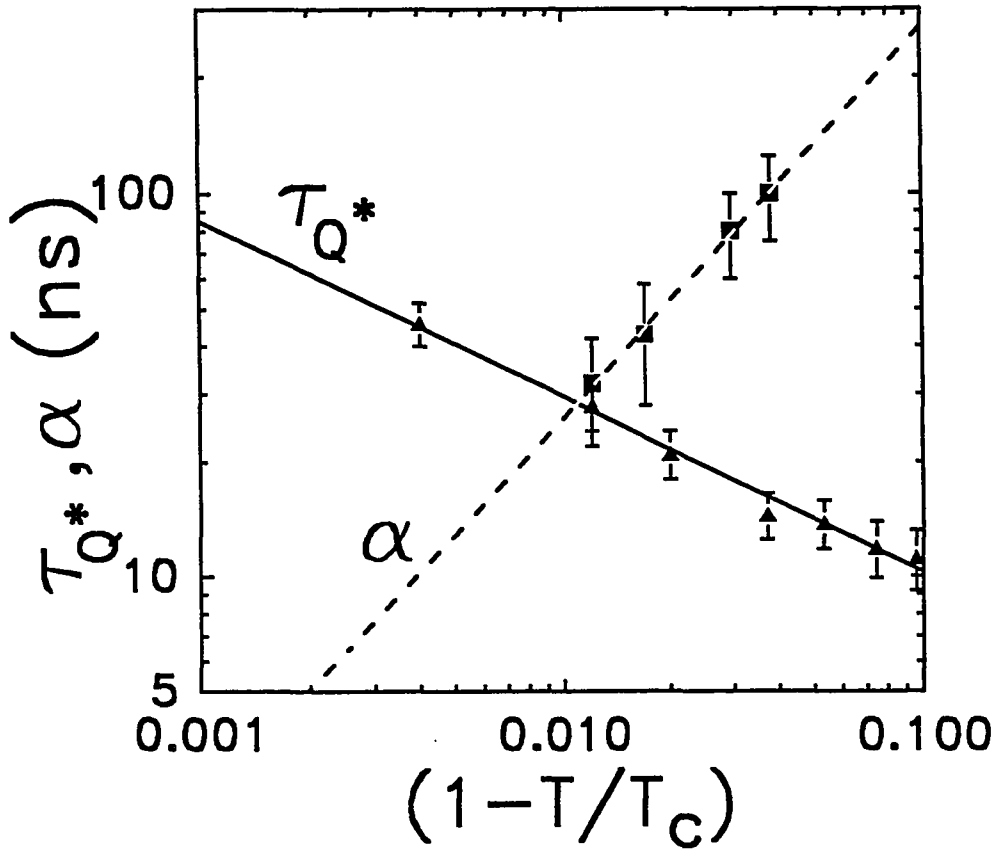

Figure 3.8 - α, the IVQ* transport coefficient, and τ_Q^* plotted against $(1-T/T_c)$.

charge imbalance in the presence of pairbreakers like supercurrent. It is possible, though unlikely, that in the dirty limit the temperature dependence of α is $(1 - T/T_c)$.

In the analysis of the data, we have assumed that the supercurrent is uniformly distributed throughout the cross-sectional area of the sample strip. This is clearly an approximation and not entirely valid. A superconducting ground plane was used to insure uniformity. Also the sample thickness is smaller than the magnetic penetration depth, which should lead to uniform flow. However, as the sample is cooled some pinching off of the current is expected, which would mean that our estimate of $\vec{v}_s$ is too large, causing us to overestimate α at low temperatures. We have not measured the magnetic penetration depth in our films, and can not adjust for this effect quantitatively. However using standard measurements in aluminum, this correction is small in our experiment.

Despite this difficulty with the temperature dependence, we are convinced that we have observed the IVQ* effect. Our confidence is based on the linearity of the generated charge imbalance with applied supercurrent, and electric field.

Chapter 4

HIGH TEMPERATURE SUPERCONDUCTING DEVICES

4.1 Overview

Ever since the discovery of superconductivity by Kamerlingh Onnes in 1911, scientists have been searching for material with higher and higher transition temperatures. This steady search culminated in the mid 1960's with the A-15 phase superconductors. From that time until recently all attempts to find superconductors with higher T_c have failed. The discovery of an oxide superconductor with an anomalously high T_c, BaPbBiO [24], stimulated interest in oxide superconductors. In 1986 Bednorz and Müller [25] published their results showing clear signs of superconductivity at 30 K in La-Ba cuprates, and the race was on. Very rapidly Wu et al. [26] discovered superconductivity at 90 K in $YBa_2Cu_3O_{7-x}$. This discovery was perceived as a very important for the development of technologically useful superconducting devices. For the first time, a superconductor could be cooled below its transition temperature by an inexpensive and safe cryogen, liquid nitrogen. This discovery is also very interesting scientifically. It had been thought for some time that superconductivity at these temperatures is impossible. The mechanism for superconductivity in these materials is still an open question. More recently, other high-T_c materials have been found. Maeda *et al.* [27] discovered the BiSrCaCuO system, which is most interesting because of the variety of superconducting phases it possesses, including

one with a transition temperature of 110 K. Sheng and Hermann [28] then discovered the TlBaCaCuO system, which again has a large number of superconducting phases, one of which is superconducting at 125 K. Other new materials have also been discovered including $Ba_{1-x}K_xBiO_3$ [29] and $Nd_{2-x}Ce_xCuO_4$ [30].

The structure for $YBa_2Cu_3O_{7-x}$ and BiSrCaCuO is shown in Figure 4.1. These materials are very different from previously studied superconductors. An excellent review of their properties is given by Ginsberg [31]. These materials are conducting ceramics - a rare combination of properties. The normal-state resistivity is at least an order of magnitude higher than most conventional superconductors, and the carrier number density is several orders of magnitude lower than conventional superconductors. Hall measurements show that normal-state transport is by holes, not electrons. However, the Ce materials show electron conduction. One of most striking features of these materials is their anisotropy, which is clear in the crystal structure. The two dimensional copper-oxygen planes are responsible for superconductivity in these materials. There is a large anisotropy in the electrical properties as a result of these planes. The critical current density (J_c) and Ginzburg-Landau coherence length (ξ) are much larger in the planes than perpendicular to them. Also the number of Cu-O planes plays a role in the superconductivity. In both the Tl and Bi systems, phases with one Cu-O plane (n=1) have a transition temperature near 40 K. The n=2 phase has a transition near 80 K, and the n=3 phase has a T_c above 110 K.

An important step in realizing high T_c superconducting devices for

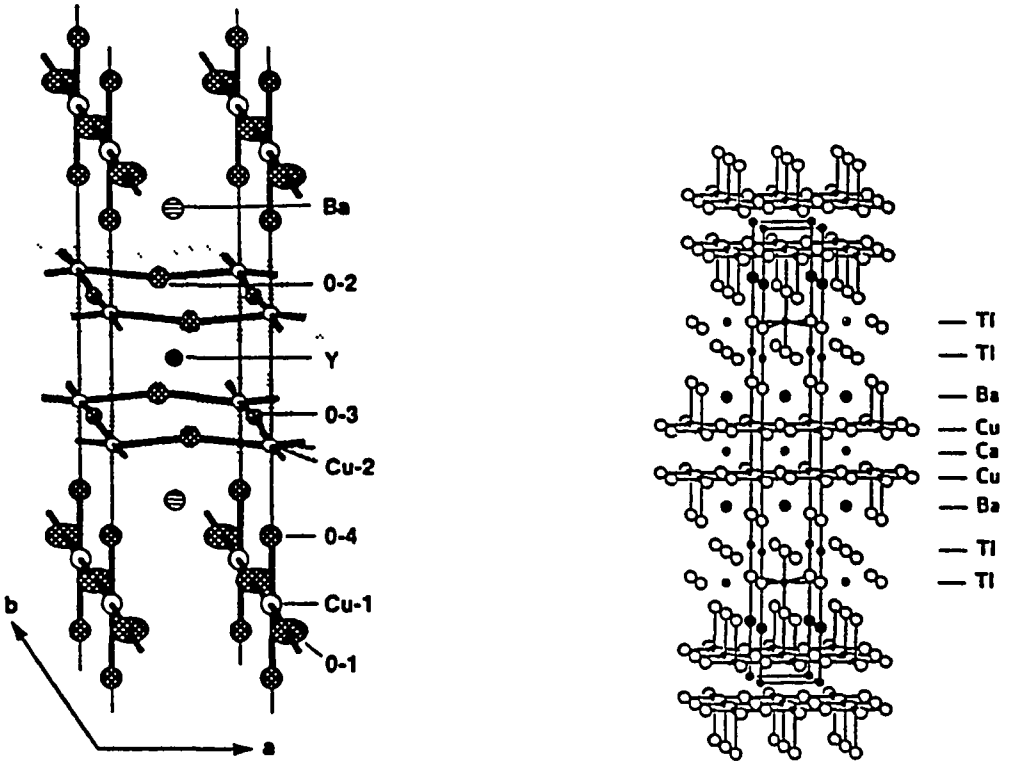

Figure 4.1 - Crystal structure of $YBa_2Cu_3O_{7-x}$ and $Bi_2Sr_2CaCu_2O_8$ (replace Tl with Bi) superconductors. Figure taken from reference [31].

fundamental scientific measurements and technological applications is the development of high quality thin films. Much work has been done to this end. The first successful films were made by multiple source e-beam evaporation [32,33]. These films were made by evaporating elemental copper, yttrium, and barium, to yield an amorphous mixture in the correct stoichiometry. This mixture was then heat treated in flowing oxygen. Under the right conditions, this procedure yields a thin film with the correct crystal structure and oxygen stoichiometry. Very quickly it was found that it was possible to create thin films by many other methods. These include single source sputtering [34,35] - that is sputtering from a target that contains all the needed elements, multiple source sputtering [36,37], ion beam deposition [38], pulsed laser deposition [39], and chemical spin-on methods [40,41]. Almost every thin film deposition method known has been made to work with some degree of success.

An important consideration for successful film growth is the choice of substrate. Because of the high temperatures involved in the heat treatment - typically 900°C - only certain substrates can be used. For example the diffusion of copper into silicon makes it nearly impossible to grow $YBa_2Cu_3O_{7-x}$ on silicon without the use of some intermediate buffer layer [42]. Similar problems occur with sapphire substrates. As a result commonly used substrates include MgO (100), yttria-stabilized ZrO_2 (YSZ) (100), and $SrTiO_3$ (100). Both YSZ and $SrTiO_3$ have an added advantage: they are somewhat lattice matched to $YBa_2Cu_3O_{7-x}$ which is an aid to epitaxial growth. As the solid state reaction that converts the amorphous mixture to $YBa_2Cu_3O_{7-x}$ occurs, the substrate acts as a template

for growth allowing epitaxial ordering of the grains.

A major difficulty in the multiple source deposition methods is the reactivity of barium. Elemental barium exposed to the air will rapidly form many oxides, hydroxides and carbonates of barium. The surface of metallic barium will rapidly change from a shiny metallic gray into a white powder. Similarly the as-deposited films made from elemental barium are very reactive with air and water. Mankiewich *et al.* [43] found a solution to this problem. Instead of elemental barium, they used BaF_2 as their evaporation source. At temperatures near 800°C, BaF_2 sublimes molecularly. These temperatures are easily attainable using either e-beam or thermal evaporators. The deposited BaF_2 film, while somewhat reactive with water, is not nearly as reactive as elemental barium. Similarly the as-deposited Y-BaF_2-Cu mixtures are very stable. The conversion of BaF_2 to BaO is produced by the following reaction [44]:

$$BaF_2 + H_2O \rightarrow BaO + 2HF. \qquad (4.1)$$

The above reaction requires the introduction of water vapor into the furnace during annealing. The Gibbs free energy for the above reaction can be calculated as a function of temperature and H_2O and HF partial pressures. Conveniently, the reaction is exothermic for temperatures in the desired range when a suitable ratio of H_2O to HF partial pressure is maintained. Another reaction helps this ratio by reducing the HF partial pressure:

$$SiO_2 + 4HF \rightarrow SiF_4 + 2H_2O. \qquad (4.2)$$

In other words, the presence of silica helps drive reaction 4.1 by decreasing the HF concentration and increasing the water concentration. Happily the walls of most tube furnaces, including ours, are made of fused silica. This use of BaF_2 has made the production of films a much more reliable business. The key disadvantage to this method is that it is impossible to develop an *in-situ* process using BaF_2, and the films must always be post-annealed.

A topic of much recent interest is the production of films by *in-situ* methods, that is films that are superconducting as deposited. One reason for this interest is difficulties in making high quality films by methods that require a post-deposit heat treatment. During the course of the solid state reaction that occurs during the heat treatment, the volume of the film changes. This volume change can cause cracking and the precipitation of non-superconducting phases in the grain boundaries. Also, the high temperatures required to attain a superconducting film generally causes a rough surface morphology and interdiffusion with the substrate. A smooth surface morphology and the absence of non-superconducting grain boundaries are important for the development of high quality devices.

To this end, many groups have been developing *in-situ* deposition processes. The main features of these processes have been deposition onto a heated substrate with a typical temperature of 700°C, and the use of some type of oxygen source. The best way to incorporate oxygen into the growing films is still not known, but many methods have been used with some success. Simple methods have been tried such as depositing in

a large O_2 or NO_2 partial pressure [45,46]. More complex methods have had somewhat more success. These include the use of ozone [47], or rf and microwave plasmas used to generate atomic oxygen [48]. The highest quality films have been made by three different *in-situ* techniques, again showing that perhaps any deposition process can be made to work. These films have been made by three source e-beam evaporation [48], single source dc magnetron sputtering [49], and pulsed laser deposition [50].

Although the development of high-quality thin films is still in its early stages, from the very beginning attempts have been made to fabricate various devices from these films. Superconducting devices made from high T_c materials are desirable for both fundamental scientific studies and technological applications. With a high quality Josephson tunnel junction one could measure the gap energy, the quasiparticle density of states, and perhaps even the phonon density of states. With two junctions one could make a SQUID capable of operation at higher temperatures, which might be useful in sorting out the details of the flux dynamics in these materials. From a technological standpoint, a high quality junction could be used as a mixer perhaps capable of operating at frequencies higher than 1 THz. The suspected large gap in these materials should lead to very fast switching times if digital devices could be made. Also, a high temperature SQUID would be useful for studying a variety of systems. Another technological area of great interest is bolometers. In theory it is possible to make bolometers more sensitive than those now available, and still operating above liquid nitrogen temperatures. The prospect of these results has prompted much

work trying to develop devices.

There are many practical difficulties in making high-quality devices from these materials. One obstacle is the surface morphology of these materials. Films that are heat treated after deposition are generally very rough and clean interfaces between films will be difficult to achieve. This problem is largely solved by *in-situ* films. A more difficult problem is the very short coherence length in these materials. Typically, junctions are made by overlapping two superconducting films with a thin insulator between them. With conventional superconductors, the coherence length is large compared to the size of the of imperfection at the interface, and so the interface between the two films need not be atomically perfect. However in the high T_c materials, the coherence length can be smaller than the unit cell, so that the film must retain its superconducting properties right up to the surface, and the interface must be nearly atomically perfect. Superlattice researchers commonly achieve such perfection in other materials, but this problem has yet to be addressed in these materials.

Attempts to make junctions and devices with high T_c materials are easily divided into two categories: natural junctions and artificial junctions. The natural junctions are devices that are made by exploiting the naturally occurring grain boundaries that occur in many of these films. Artificial junctions are those that are made by fabricating some type of structure to yield a junction or junction-like configuration.

The first device made in $YBa_2Cu_3O_{7-x}$ was a SQUID by Koch *et al.* [51] This SQUID was fabricated by patterning a small loop in a polycrystalline film of $YBa_2Cu_3O_{7-x}$ and using the weak-link nature of the coupling

between grains. Similar devices have been made by lift-off processing [52]. Higher quality devices have been made by the IBM group by using pulsed laser patterning to pattern SQUIDs and weak links across single grain boundaries in highly epitaxial films [53]. They have also succeeded in making SQUIDs in polycrystalline TlBaCaCuO. The noise performance of these SQUIDs at 77 K rivals the performance of commercially available SQUIDs operating at 4 K. The reasons for the superior performance of the Tl-based SQUIDs over the $YBa_2Cu_3O_{7-x}$ based SQUIDs are unclear.

The attempts to make artificial junction-like structures have been far less successful to date. This situation may change with the current developments in high-quality film growth. There have been several attemps to make tunnel junctions using normal metal or "conventional" superconducting counterelectrodes [54]. In all of these attempts, no supercurrent is seen, and the only gap observed is that of the counterelectrode. Mankiewich [55] has had some promising initial results making proximity effect junctions.

4.2 Thin Film Development

We have developed processes for making both $YBa_2Cu_3O_{7-x}$ and BiSrCaCuO thin films. The $YBa_2Cu_3O_{7-x}$ films are made by a co-deposition process involving a mix of dc magnetron and thermal evaporation sources. The BiSrCaCuO films are made by sequential evaporation process. Both of these methods involve a post deposition heat treatment. More recently, we have worked on an *in-situ* pulsed laser deposition method. The procedures used for making these films and measurements of film quality

are presented in this section.

4.2.1 $YBa_2Cu_3O_{7-x}$

The co-deposition system used for making $YBa_2Cu_3O_{7-x}$ thin films is a modified Sputtered Films S-Gun Research system. Before modification, the system was equipped with two 1.5 inch dc magnetron sputter guns and one 1.5 inch rf magnetron sputter gun. The system is pumped by a turbo-molecular pump and has a base pressure of 5×10^{-7} Torr. Substrates are held on a rotating planetary that passes over the guns allowing uniform deposition over large areas. The system is also equipped with three quartz-crystal deposition rate monitors, which allow independent monitoring of the three sources. A schematic representation of this process is shown in Figure 4.2. The yttrium and copper were sputtered using the two d.c. sputter guns. The copper target had a purity of 99.99%, and the yttrium target had a purity of 99.9%.

Because of the reactivity of Ba with the atmosphere, we decided not to sputter it. A barium sputter target is expensive and would quickly degrade into powder. Instead, a small thermal evaporation source was designed and built to fit inside the chamber. In this way, a small amount of barium could be loaded into the chamber for evaporation, and any unused barium could be elminated from the source by evaporating it to completion. The barium source consists of a small Mo crucible with a tungsten filament embedded in the wall. The tungsten wire is insulated from the Mo by alumina tube. A thin-walled stainless steel heat shield surrounds all but the mouth of the crucible. Current is applied to the filament through Kovar electrical feedthroughs. The source was then connected to a Variac auto-transformer. The filaments typically had a

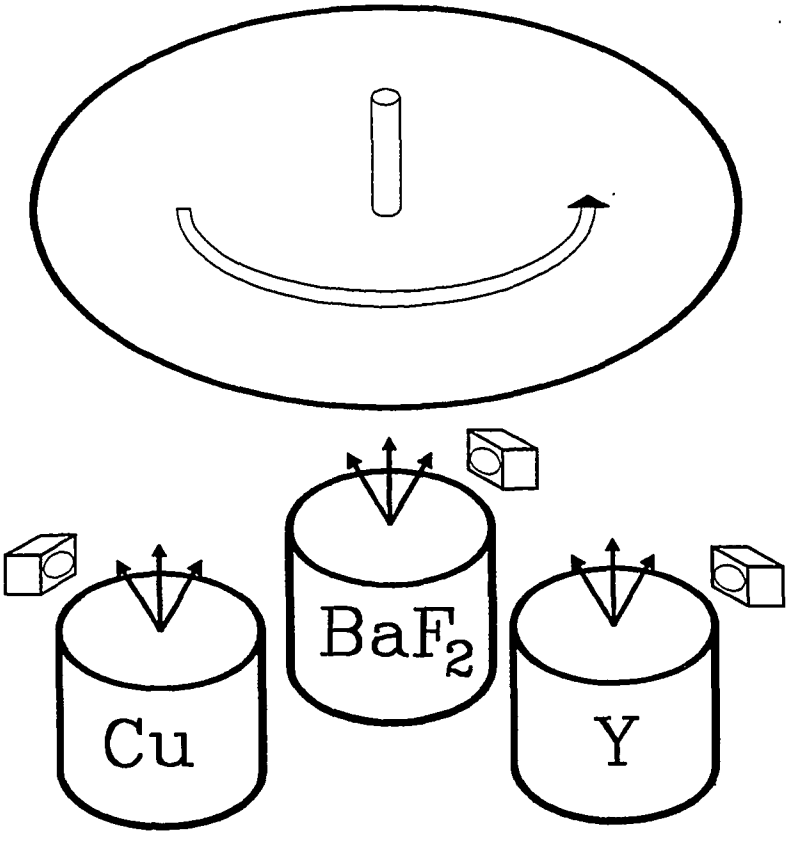

Figure 4.2 - Schematic representation of the multi-source deposition system used, showing sources, rate monitors and rotating substrate holder.

resistance of 4 Ω, and an applied power of 400 W caused the interior of the crucible to reach temperatures higher than 800°C.

Although the thermal source was conceived with the evaporation of barium in mind, we quickly started using it with BaF_2. A few films were made using metallic barium, but the transition temperature of these films were never greater than 50 K. In Mankiewich's paper [43] reporting his use of BaF_2, the authors made similar comments about being unable to attain T_c over 60 K using metallic barium. They reported no similar problems when using BaF_2. As will be shown later, we have also obtained very good results using BaF_2.

One difficulty with mixing sputtering and evaporation processes is the presence of gas required for the plasma driven sputtering process. Generally this gas is argon, although other gases can be used. Typical gas pressures used for sputtering are in the range of (1-100) $\times 10^{-3}$ Torr, and depend on the design of the sputttering source. While evaporating in the presence of gas, the evaporants are scattered in random directions reducing the flux of evaporant at the substrate. In our system, we are using magnetron sputter sources, which are capable of operating at much lower pressures than other sputtering sources. As the name implies, magnetrons use a magnetic field to cause the electrons in the plasma to move in spiral orbits, and thus have a much shorter effective mean free path for ionizing gas molecules. This enables magnetrons to work at lower gas pressures. For most of work we used an operating pressure of 1.5×10^{-3} Torr. At this pressure the mean free path of the gas molecules is 10 cm. This length is smaller than the distance between the barium source and the substrate. As a result scattering of

the evaporant by the sputtering gas is not a serious problem.

During the course of a co-deposition process, the rate of deposition from each source is normally controlled independently. Many commercial deposition rate monitors also have a control function. That is, they have some output signal, and have a feedback loop - adjusting the size of the output signal to maintain the desired deposition rate. The crystal monitors that we use (Inficon XTC) have this feature, but we have had difficulty in using it with the barium source. Because of design constraints, the barium source was operated at currents very near those that cause the filament to burn out. When automatic control of this source was attempted, filaments were generally burned out very quickly. Changing filaments is a lengthy and tedious operation, so we had to find some other control method. Many of the first films were made using a human controller. In other words, the person depositing the films had to monitor three separate rate controllers and adjust the source power controls to maintain the correct stoichiometry. In this age of high technology, there must be a better way.

To solve this problem we made a ratiometric deposition controller. The purpose of this controller is to monitor one of the sources (the master) and adjust the deposition rate of the other sources (the slaves) to achieve the correct stoichiometric ratio. To accomplish this we used an IBM AT type computer. The computer was interfaced to the existing crystal rate monitors. The control software was then written. This software was designed to read the rate of the master once every second. It then calculates the desired rate for up to three the slaves based on a moving average of the master rate, and outputs this new setpoint to the

slaves. The software also displays instantaneous and average statistics for the deposition in real time. In practice, this control system maintains the correct stoichiometry within 5% instantaneously and to better than 0.1% over the course of the deposition.

After deposition the films are brownish-black, smooth, shiny, amorphous and insulating. They need to be reacted with oxygen to form $YBa_2Cu_3O_{7-x}$. We used a conventional tube furnace for the heat treatment. This furnace consists of a quartz tube surrounded by the heating elements, with a removable cap at one end, and gas connections at the other end. Throughout the heat treatment, oxygen was flowing through the tube at a flow rate of 2-5 SCCM. To assist in the conversion of BaF_2 to BaO, the oxygen was bubbled through distilled water during the highest temperature portion of the heat treatment. The optimal heat treatment cycle was determined empirically. The films were rapidly heated to 900°C and held there for 20-30 minutes. It was then cooled at 120°C/hour with 1 hour soaks at 700°C and 450°C. We believe the soak at 700°C assists in the tetragonal to orthorhombic phase transition, and the soak at 450°C allows the uptake of additional oxygen. We also found that the rapid initial heating is important. This rapid heating minimizes the time the sample is near the highest temperatures. It is important to keep this time short to minimize film-substrate interactions.

The superconducting transition for one of the best films made by this method is shown in Figure 4.3. The films exhibit a linear resistivity above T_c, and a sharp transition beginning at 91 K and obtaining zero resistance by 86 K. Resistance was measured using a four probe ac technique with a 100nA excitation current. Temperature was

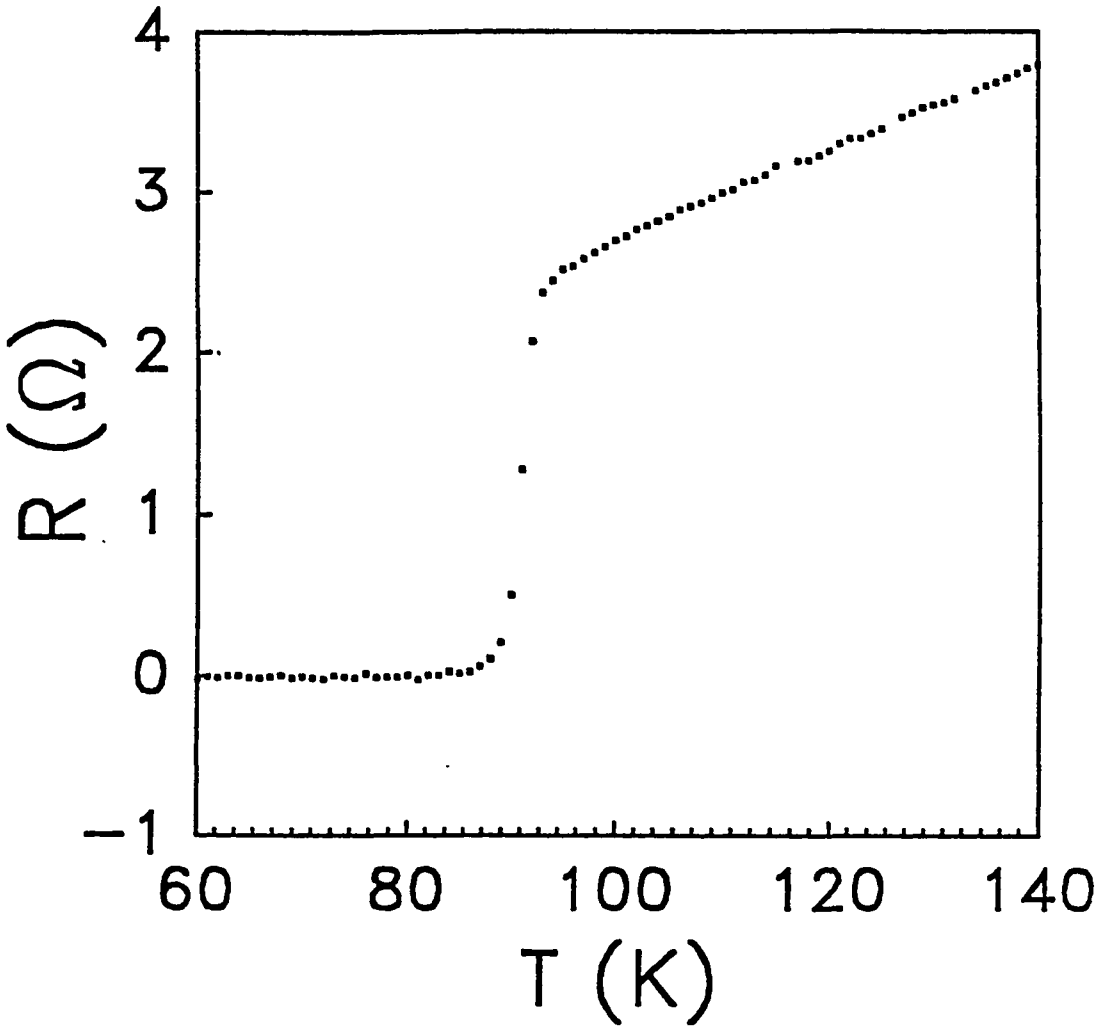

Figure 4.3 - Resistive transition of $YBa_2Cu_3O_{7-x}$ thin film made by multiple source deposition.

measured with a Si diode thermometer calibrated in the range 1.5-300 K. The data were taken under computer control warming at a rate of 2 K/min. over the transition region. We were able to make many films with transitions resembling this one, but many films had much broader transitions. We attribute the lower quality films to difficulty in stoichiometry control, and to contamination in the vaccuum system, which is used by many other people to deposit other materials.

The critical current density, J_c, was also measured on many films. In order to make this measurement, it is necessary to pattern the film with a constriction of known size. The details of this process will be presented in the section on devices. We obtained values of J_c between of 10^5-10^6 A/cm^2 at 4 K. These values are comparable to values obtained by others using similar deposition methods. Much higher values of J_c have been found in *in-situ* films however.

As stated earlier, films made with a post deposition heat treatment are very rough and textured. An electron micrograph of one of these films is shown in Figure 4.4. As this picture shows, the films are polycrystalline with the individual grains epitaxially ordered. This "basket weave" pattern is caused by triaxial epitaxial ordering. That is, the grains of the film are aligned with two of their three principal crystal directions parallel to the substrate. We have found that we can modify this microstructure somewhat by adjusting the stoichiometry. We have made smoother, mostly *c*-axis oriented films by increasing the Ba concentration by a few percent. These films are still quite rough however.

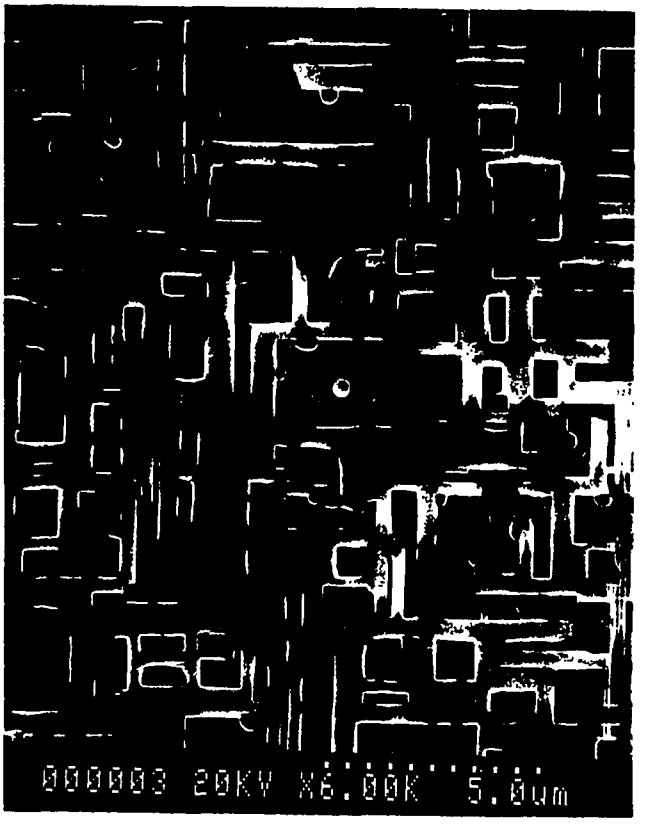

Figure 4.4 - Electron micrograph of $YBa_2Cu_3O_{7-x}$ thin film made by multiple source deposition.

4.2.2 BiSrCaCuO

We decided to make BiSrCaCuO for several reasons. First it had been reported that BiSrCaCuO is less sensitive to water than $YBa_2Cu_3O_{7-x}$, which makes the fabrication of devices easier, and makes the resulting devices more robust. Another reason for working with the Bi system is the higher T_c phase it possesses. Our BiSrCaCuO films were made by a much simpler process than the $YBa_2Cu_3O_{7-x}$ films. There was no existing four source co-deposition system available, so we decided to make films by sequential deposition. Other groups [56,57] have employed this technique successfully in $YBa_2Cu_3O_{7-x}$. This technique is shown schematically in Figure 4.5. The metallic constituents Cu, and Bi, and the fluorides CaF_2 and SrF_2 are thermally evaporated in a stack of 20 layer (5 repetitions of the basic four layer stack of SrF_2, Cu, CaF_2, and Bi). Fluorides of Sr and Ca were chosen for the same reasons BaF_2 was chosen. All evaporation materials had a purity of at least 99.99%.

The depositions were carried out in a diffusion pumped thermal evaporator. This system is equipped with four separate thermal evaporation positions and one crystal thickness monitor. The material to be evaporated was placed in tungsten dimple boats. The system was pumped to its base pressure of 1×10^{-6} Torr. Flowing oxygen was admitted to the chamber to reach a pressure of 1×10^{-5} Torr. This oxygen was used to partially oxidize the copper and bismuth. The film was built up layer by layer until a thickness of 500 nm was reached. The thickness of each individual layer was chosen to satisfy the stoichiometric constraints. Generally, we wanted the films to have a stoichiometry of $Bi_2Sr_2CaCu_2O_8$. We found that we could make superconducting films with a wide range of

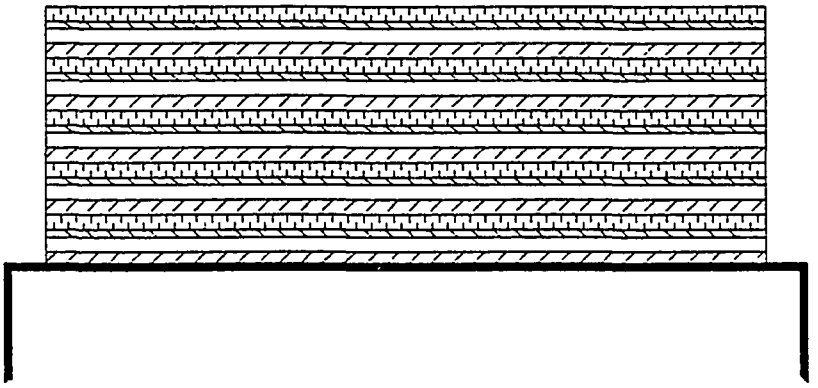

Figure 4.5 - Schematic of sequential deposition used for BiSrCaCuO showing five repetitions of the four constituents: SrF_2, Cu, CaF_2, and Bi.

stoichiometry. This is very different from $YBa_2Cu_3O_{7-x}$, where superconducting films are obtained only for a very narrow range of stoichiometry.

We chose to use MgO (100) substrates for these films. Early work showed that no real advantage was gained by using $SrTiO_3$ (100) with the Bi system. Also the price of MgO is an order of magnitude less than that of $SrTiO_3$.

Much like $YBa_2Cu_3O_{7-x}$, the BiSrCaCuO films are smooth and shiny as deposited, however they are conducting. This conductivity is due to the thick layers of Cu and Bi in the film. These films also need to be reacted in oxygen to form the superconducting phase. The films were heated in a tube furnace similar to that used for $YBa_2Cu_3O_{7-x}$. Wet oxygen was used to convert the CaF_2 to CaO and the SrF_2 to SrO. The heat treatments for BiSrCaCuO and $YBa_2Cu_3O_{7-x}$ are very different. We found the optimal heat for BiSrCaCuO treatment to be a slow ramp to the final temperature (400°C/hour) followed by a 20-30 minute soak at 800°C, and a rapid cool to room temperature. A slow warming cycle is found to be very important. We feel that the reason for this is the large amount of metallic bismuth in the film. Metallic bismuth has a melting point near 300°C, so it is necessary to oxidize the bismuth as much as possible to prevent liquid bismuth from flowing.

The superconducting transition for these BiSrCaCuO films is shown in Figure 4.6. These films usually show an onset between 90 and 100 K, and show zero resistance between 80 and 84 K. The resistivity of these films is roughly 200-300 $\mu\Omega$-cm at T_c. Using transport measurements, J_c was determined to be $1\text{-}5\times10^5$ A/cm^2 at 4 K. These resistivity and current

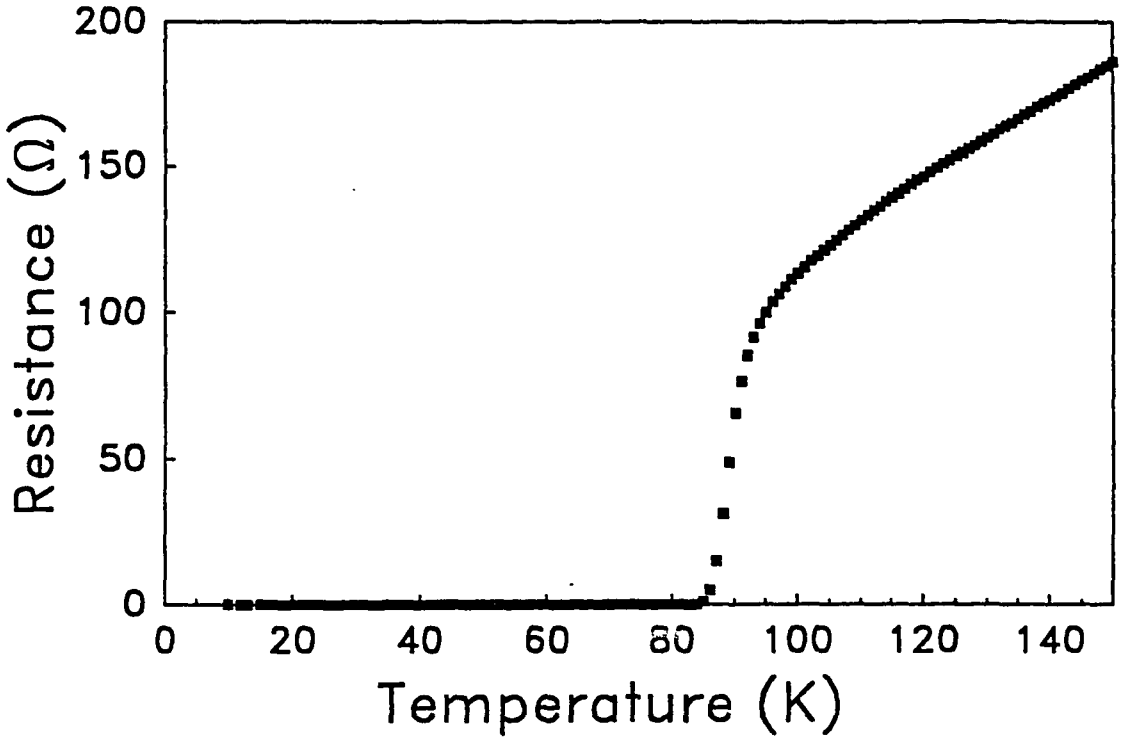

Figure 4.6 - Resistive transition of BiSrCaCuO thin film.

density values approach those measured in the best films made. It is surprising that such a simple approach can yield such high quality films.

Figure 4.7 is an electron micrograph of a BiSrCaCuO film. The grain structure is characteristic of BiSrCaCuO films. The grains show a plate-like structure. X-ray diffraction (Figure 4.8) data show that the films are *c* axis oriented. The only lines observed in this diffraction pattern are the [0 0 ℓ] lines for $Bi_2Sr_2CaCu_2O_8$. This does not mean that the films were completely single phase. Small amounts of other phases would not be detected by this X-ray technique. Because of the high onset temperature of these films, some of the n=3 phase must be in the samples. Unlike our $YBa_2Cu_3O_{7-x}$ films, these films are randomly oriented with respect to the *a* and *b* axes.

4.2.3 Pulsed Laser Deposition

A stated earlier, it will be very important for future work, both scientific and technological, to develop high quality *in-situ* films. One very promising technique for depositing high quality thin films is pulsed laser deposition (PLD). This technique, developed primarily by Wu, Vanketesen *et al.* [39], uses a laser to evaporate from a sintered target of superconductor. This technique has been used for other materials for many years, but has not had the advantages over other processes that it appears to have with the oxide superconductors. A schematic of PLD is shown in Figure 4.9. A high energy pulsed laser is directed at a target of sintered superconductor in a vacuum chamber. An oxygen atmosphere is admitted to the chamber at a pressure of 1 - 200 mTorr. A heated substrate at 600 - 800°C is placed 3 - 10 cm away from the target.

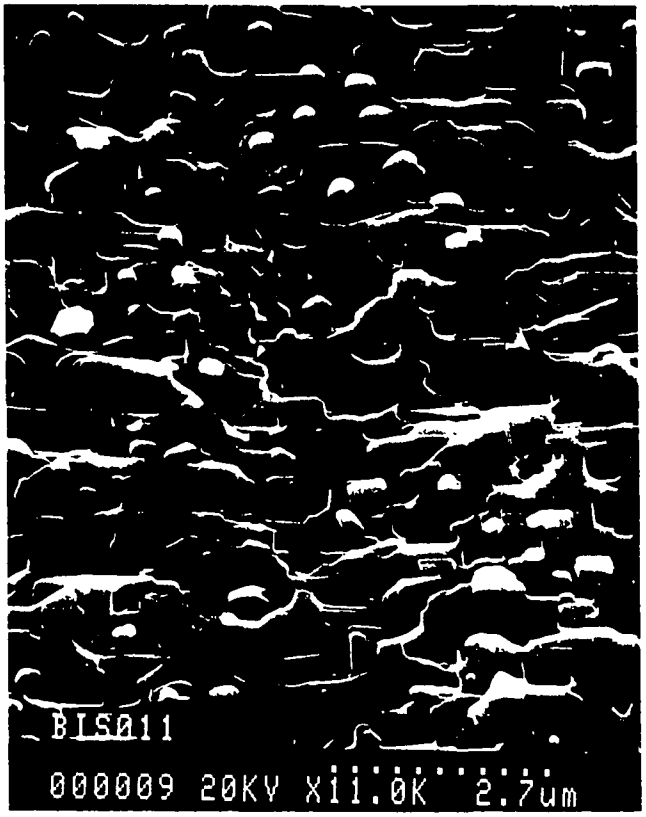

Figure 4.7 - Electron micrograph of BiSrCaCuO thin film.

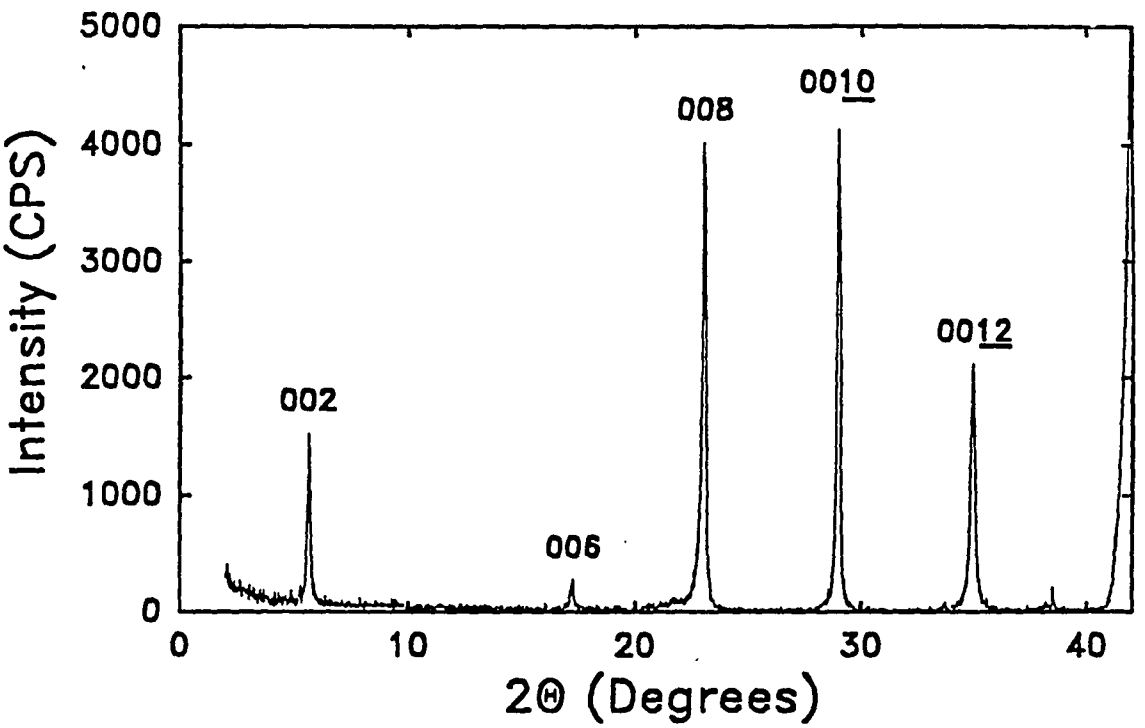

Figure 4.8 - X-ray diffraction data for BiSrCaCuO thin film.

This is a very simple and inexpensive process, and yet it yields spectacular film quality. It does have one disadvantage for technological applications: it is difficult to make films larger than 1 cm^2 by this process. For research applications, this is not a limitation.

A variety of different lasers has been used for this process, however the process seems to work best with deep UV lasers. The short wavelength illumination interacts with a smaller target volume, causing the target heating to be more localized. The best results initially were obtained with excimer lasers using both ArF (193 nm) and KrF (248 nm). More recently [58], Nd-YAG lasers have been used in frequency doubled and frequency tripled mode with equal success. The pulse times used are laser dependent and between 10 and 50 ns. Generally the targets are illuminated with a fluence of 1 - 5 J/cm^2.

Although the exact nature of this process is still not understood, Vanketesan [59] has done measurements that explain some of the process. He found that during the course of PLD there are two distinct components to the evaporation. One component is non-stoichiometric and shows a $\cos(\theta)$ angular dependence. This is precisely what one would expect from point source evaporation of the target. A non-stoichiometric films is expected because the elements all have different vapor pressures and sticking coefficients. He also found that there was a forward directed stoichiometric component to the deposition. The angular dependence of this forward component is sharper than $\cos^{11}(\theta)$. Several models have been proposed to explain this second component, and the reasons for it are still unresolved.

The system we built to do PLD is very much like the schematic shown in Figure 4.9. It is a small stainless steel vacuum chamber equipped with a 170 ℓ/s turbo-molecular pump. The target is a 1.3 cm disk of high purity $YBa_2Cu_3O_{7-x}$ powder indium soldered to a copper target holder. The target holder is mounted on a motor-driven magnetic rotary feedthrough. We are using a Lambda-Physik EMG 102 KrF excimer laser. This laser is capable of 200 mJ per pulse. The light from this laser is focused by a 30 cm focal length Suprasil quartz lens and entered the chamber through a Suprasil quartz window. A thin stainless steel capillary directs oxygen to the region just above the target. The substrates are attached to a stainless steel heater block 5 cm from the target by inorganic silver paint. The heater block is wrapped with Ni-Chrome coaxial heater wire, and surrounded by two thin stainless steel heat shields. A Chromel-Alumel thermocouple protected by an Inconel shield is placed in a thermal well in the heater block.

At this point it would be wise to state some safety precautions. Pumping a system with 100 mTorr of oxygen can be dangerous. It is very important to take adequate precautions with the pumps. A roughing pump that must pump more that 30% oxygen is subject to explosion. This is because the hydrocarbon lubricants in the pump become saturated with oxygen and "crack". When this happens, they will no longer lubricate adequately, and the pump will become very hot - so hot that the lubricant's flash point is exceeded. To avoid this problem the pump must be lubricated with a fluorocarbon or "Fomblin" type .ubricant. However, it is not sufficient to drain the pump and add the new lubricant. The pump must be completely disassembled, and all traces of the hydrocarbon

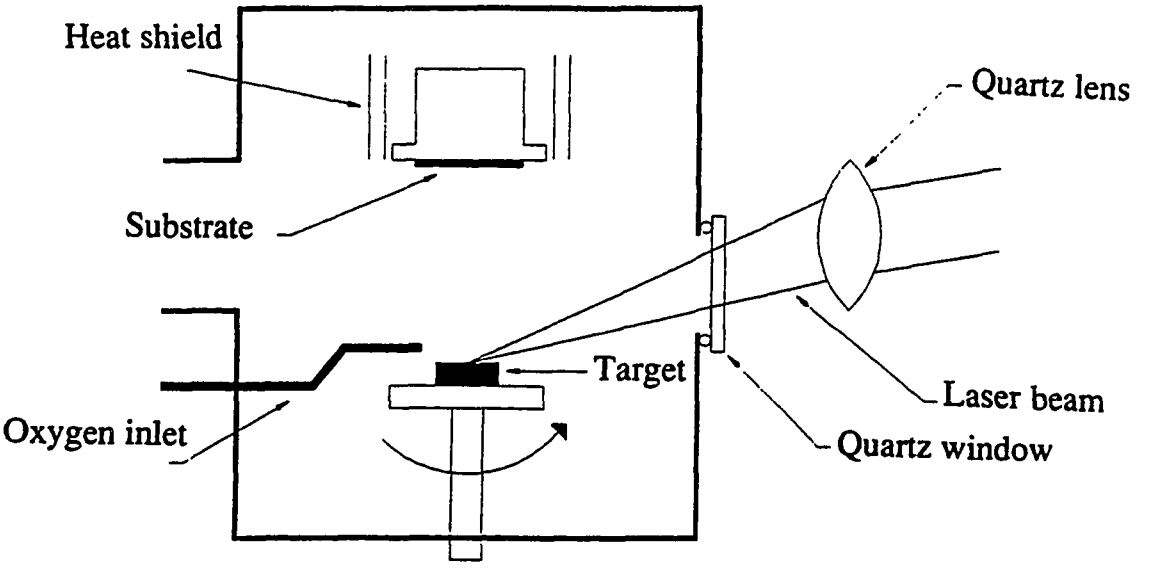

Figure 4.9 - Schematic drawing of pulsed laser deposition system.

lubricant removed. Also all the seals in the pump must be changed.

Another difficulty with working with oxygen is making a stage heater. At temperatures of 700°C and oxygen pressures of 100 mTorr, corrosion is a real problem. That is why some non-standard techniques were used in the construction of our heater. For the heating element we used Ni-Chrome coaxial heater wire. This is Ni-Chrome wire surrounded by MgO insulation and a stainless steel sheath. Connections to the wires are made external to the vacuum system, so the Ni-Chrome never sees the combination of high temperatures and oxidizing atmosphere. The stainless steel sheath will corrode with time, but the stage was designed so that it will be relatively easy to replace. Similar steps were taken with the thermocouple. The calibration of a Chromel-Alumel thermocouple will change if operated at high temperatures in an oxidizing atmosphere. The thermocouple is entirely sheathed in Inconel - a high temperature corrosion resistant alloy. The heater block and heat shields are currently made of stainless steel. After ten runs of the apparatus, corrosion of these surfaces is already apparent. New pieces will be machined from Haynes alloy 214. This nickel-based alloy is the most oxygen resistant alloy available for the temperature range used. It is ten times more oxidation resistant than Inconel and one hundred times more resistant than stainless steel.

Because of the simplicity of this process, superconducting films were achieved very quickly in this system. We have found that for our system, the best deposition parameters are a laser fluence of 2 J/cm^2, an oxygen pressure of 100 mTorr, and a stage temperature of 700°C. These parameters are similar to those used by other authors. The films are of

very high quality. A resistive transition for a film made by PLD is shown in Figure 4.10. The important features are the low resistivity, and the very narrow transition width, both features that suggest high quality films. An electron micrograph of these films is shown in Figure 4.11. These films are very smooth, and we observe no macroscopic grain boundaries. We feel this absence of grain boundaries accounts for their very large J_c. We have measured J_c as large as $x \times 10^6$ A/cm^2 at x K in these films.

4.3 Device Development

4.3.1 Patterning

Before any thin film superconducting devices can be made from a material, a way to pattern the thin film must be found. Although other approaches have been used, such as laser patterning [53], and ion implantation [51], we chose to attempt standard lithographic micro-fabrication techniques. These techniques involve the use of a light sensitive polymer, called photoresist to transfer a pattern to the films. There are two different processes that we have used, lift-off and etching.

Figure 4.12 illustrates the lift-off process. This is a pre-deposition process, meaning that the pattern is formed before the film is deposited. A thin layer (~1 μm) layer of photoresist (AZ 1350J SF) is spin-coated on the substrate. The substrate is then baked at 70°C for 30 minutes. It is then soaked in chlorobenzene for 10 minutes. This soak in chlorobenzene hardens the top layer of resist, making the undercut shown schematically in Figure 4.12 possible. The resist is then

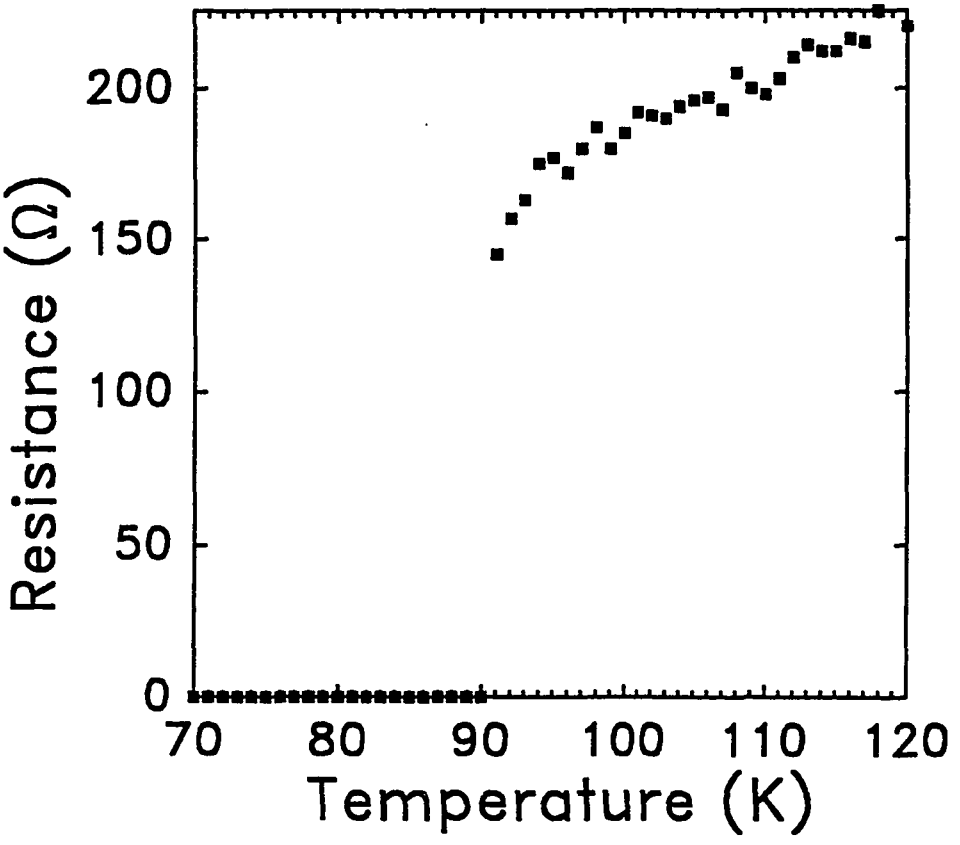

Figure 4.10 - Resistive transition of $YBa_2Cu_3O_{7-x}$ thin film made by pulsed laser deposition.

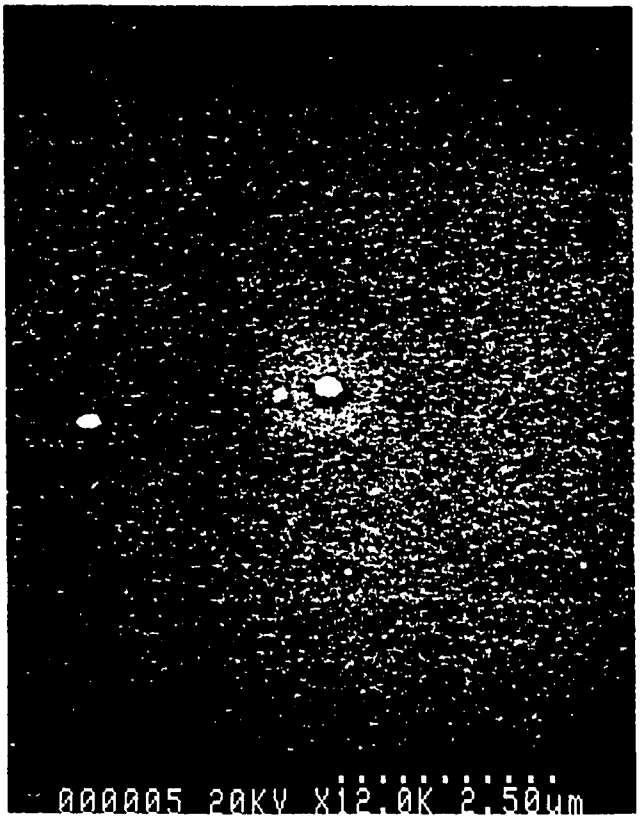

Figure 4.11 - Electron micrograph of $YBa_2Cu_3O_{7-x}$ thin film made by pulsed laser deposition showing extreme smoothness and lack of macroscopic grain boundaries.

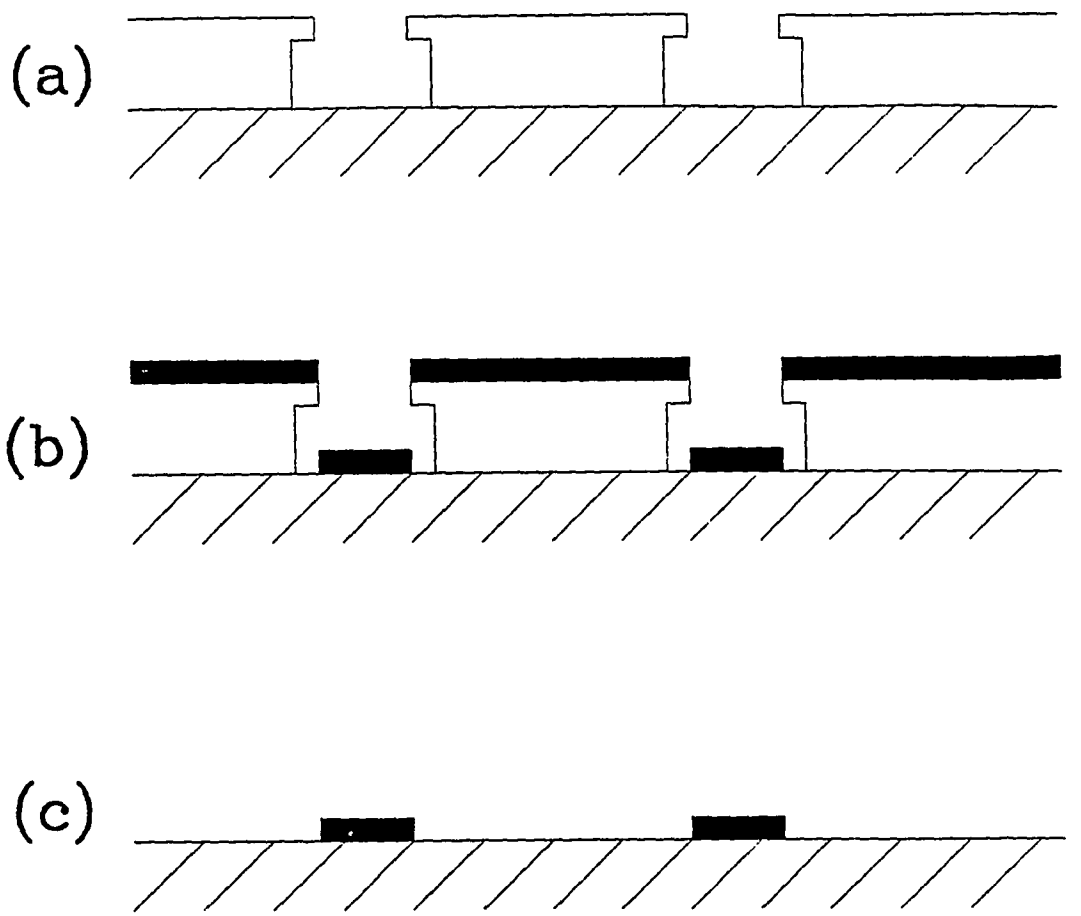

Figure 4.12 - Side view schematic of the lift-off process showing (a) patterned lift-off stencil (b) material deposited onto stencil (c) resulting structure after lift-off.

exposed with ultraviolet light through a mask. The mask is a chrome-plated piece of glass with a negative image of the pattern to be reproduced. Where the photoresist has been exposed to UV, bonds are broken in the polymer, making the exposed resist more soluble in developer. This undercut pattern in the photoresist then acts as a stencil on the substrate during deposition. After deposition the sample is soaked in acetone, which dissolves the remaining photoresist, causing the unwanted material to "lift-off". With this technique it is routinely possible to fabricate features with minimum sizes of 1μm or less.

This type of process has both advantages and disadvantages for patterning high-temperature superconductors. The biggest limitation is that lift-off can only be used for low temperature (<200°C) depositions. If the photoresist gets too hot it bubbles and cracks. At the temperatures required for *in-situ* processing, photoresist will burn. However, when used with low-temperature or post-annealed deposition, this process has a real advantage over the etch method. As stated earlier, post-annealed $YBa_2Cu_3O_{7-x}$ films are somewhat water sensitive after heat treatment. However when these films are patterned by lift-off, the films are not exposed to the water used in the lithographic process. The films are only exposed to the acetone used to remove the resist stencil. This allows us to pattern the films with little or no degradation in film quality.

For patterning *in-situ* films, or for films that have already been heat treated, a different process is called for. In this type of process material is selectively removed from the substrate in the desired pattern. A schematic representation of this etch process is shown in

Figure 4.13. Here, photoresist is spun on a substrate that is already covered with a superconducting film. The photoresist is then exposed and developed as before. The photoresist is now a protective layer over the material that is not to be removed. The material that is to be removed can now be etched in several ways. It is possible to etch the unwanted material with a weak acid solution. Because of the isotropic nature of the acid etching process, it is difficult to achieve small geometries with acid etching. Generally, dry-etching processes like ion-milling or plasma etching allow smaller geometries. In ion-milling, a collimated beam of 500 eV argon ions are directed at the sample. These ions sputter etch the exposed material. They also sputter etch the remaining photoresist, however the photoresist etches slowly. Plasma etching utilizes a similar sputter-etch process, but uses gases that are highly reactive with the material to be removed to increase the etch rate. We used ion-milling for our etching, primarily because plasma etching processes for these superconductors are still under development.

The pattern used for much of this work consists of 3 wires each with four external lead attachments. This geometry allows both resistivity and J_c to be measured. We have made this microbridge pattern with ten, five, and two micron linewidths. An electron-micrograph of a 2 μm $YBa_2Cu_3O_{7-x}$ line fabricated by liftoff is shown in Figure 4.14. A current-voltage characteristic for this line is shown in Figure 4.15. It is clear that the behavior of this line is not that of a bulk superconducting wire. A thin wire of bulk superconductor is expected to show a distinct current where a voltage appears. Instead this sample shows a slow power-law onset of voltage. This behavior is reminiscent of

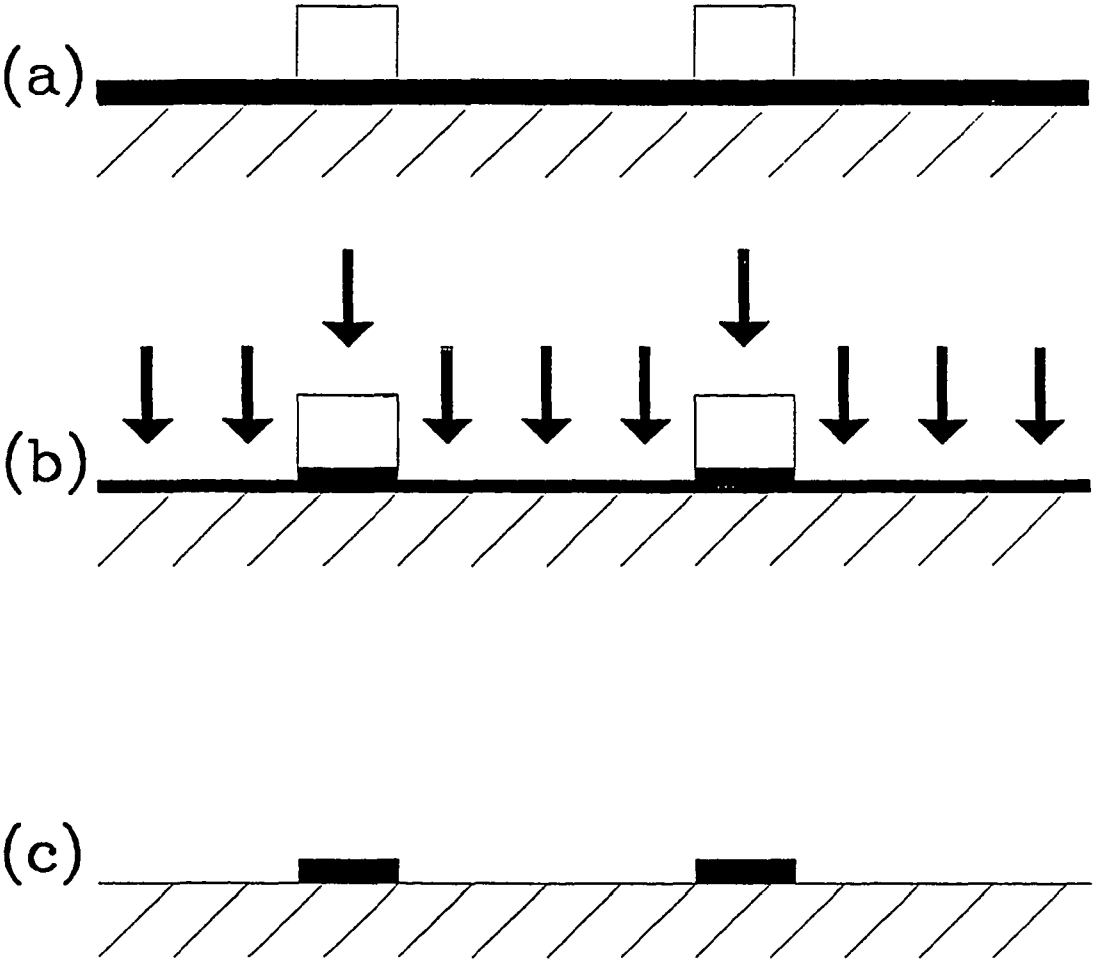

Figure 4.13 - Side view schematic of etch patterning process showing (a) deposited material with applied photoresist (b) material and patterned photoresist being subjected to etchant (c) resulting structure after etching and photoresist strip.

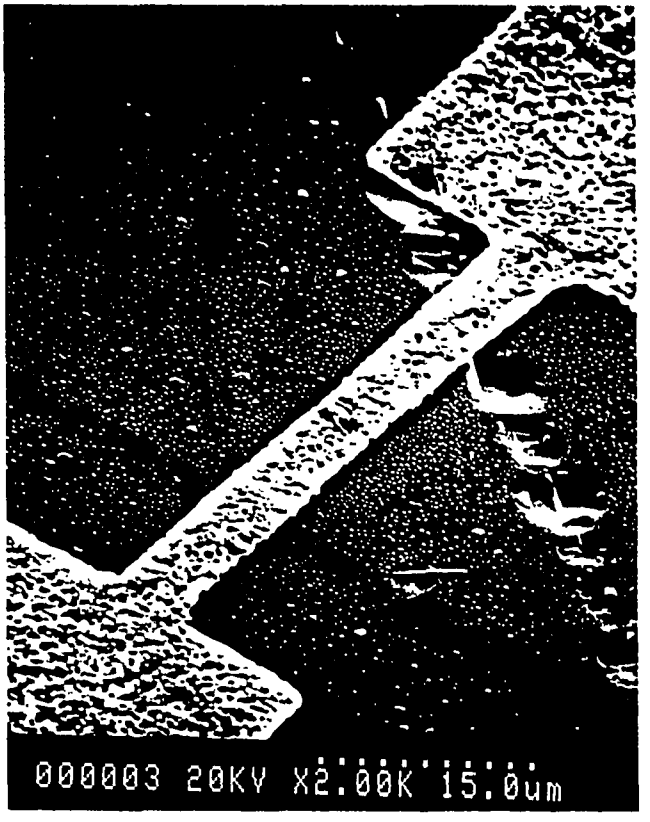

Figure 4.14 - Electron micrograph of 2μm line of $YBa_2Cu_3O_{7-x}$ line patterned by lift-off.

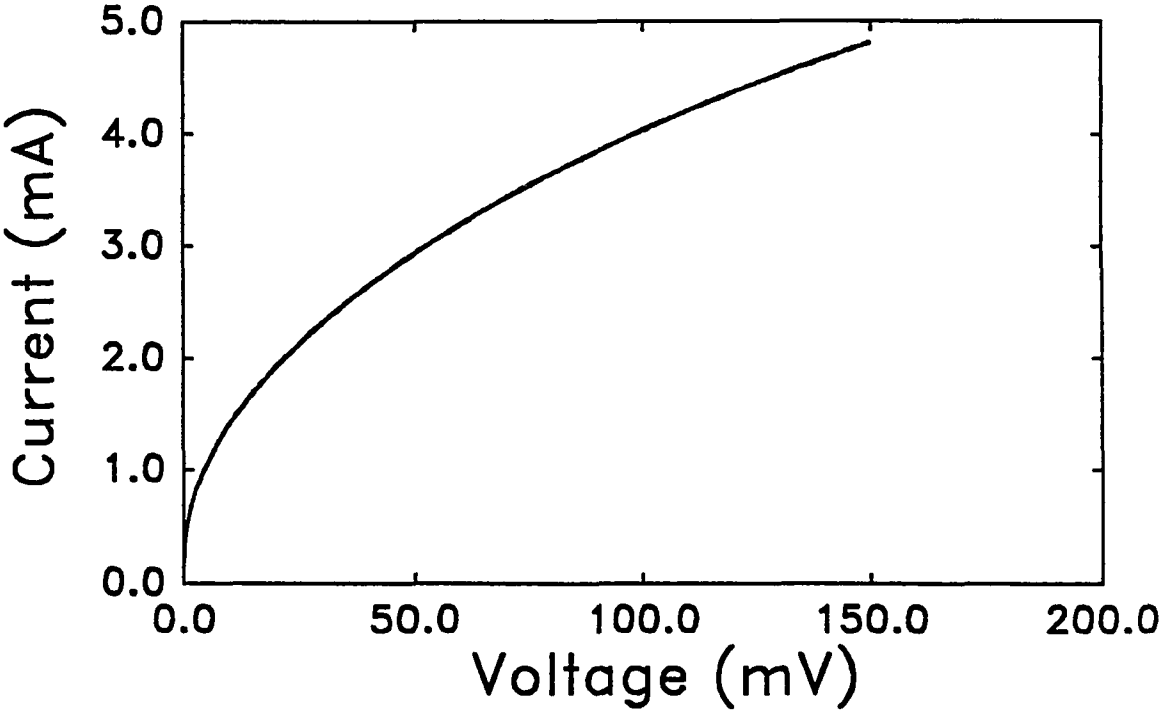

Figure 4.15 - Current-voltage characteristic of 2μm line of $YBa_2Cu_3O_{7-x}$ patterned by lift-off.

that seen in proximity-coupled superconductor arrays [60,61]. Proximity-coupled arrays are arrays of superconducting islands, with inter-island coupling provided by a normal metal. The proximity effect in the normal metal allows the entire array to become superconducting at some temperature below the superconductor's T_c. The resistance in these systems is dominated by flux flow resistance, where vortices set up by circulating currents between islands are subjected to the Lorentz force. In some ways, these arrays model a grainy superconductor. This is how we interpret the current-voltage characteristic in $YBa_2Cu_3O_{7-x}$. Further evidence for this grainy behavior is provided by the resistive transition. When the linewidth of the sample is reduced to 2μm or less, the resistive transition broadens. At these widths the microbridge is only a few grains wide.

Similar patterning has been carried out on BiSrCaCuO thin films. Figure 4.16 shows an electron micrograph of BiSrCaCuO film patterned by lift-off, and Figure 4.17 shows a film patterned by etching. A problem was discovered in patterning lift-off on the Bi system. As the micrograph shows, a needle-like growth pattern of randomly oriented grains has occurred. With smaller lines, this effect is even worse. Attempts to pattern 2 μm wide lines failed completely, yielding lines that were not continuous. We attribute this problem to an edge effect. After the lines are lifted-off, they are heat treated. At this point the metallic Bi in the film is very mobile and has a high vapor pressure. We believe that some of the Bi is leaving the film at the edges, and changing the local stoichiometry, causing the anomalous growth. As the linewidth is increased, this becomes less of a problem. Further evidence

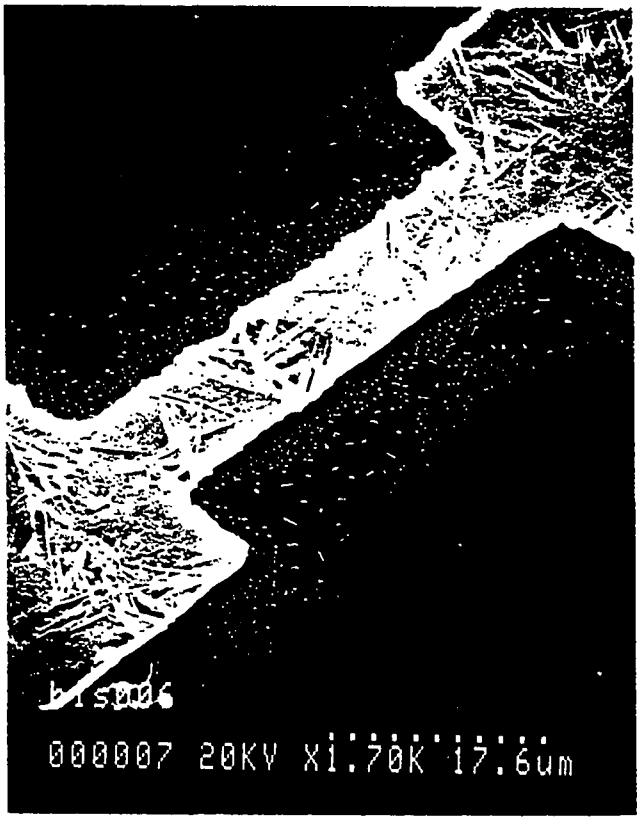

Figure 4.16 - Electron micrograph of BiSrCaCuO line patterned by lift-off.

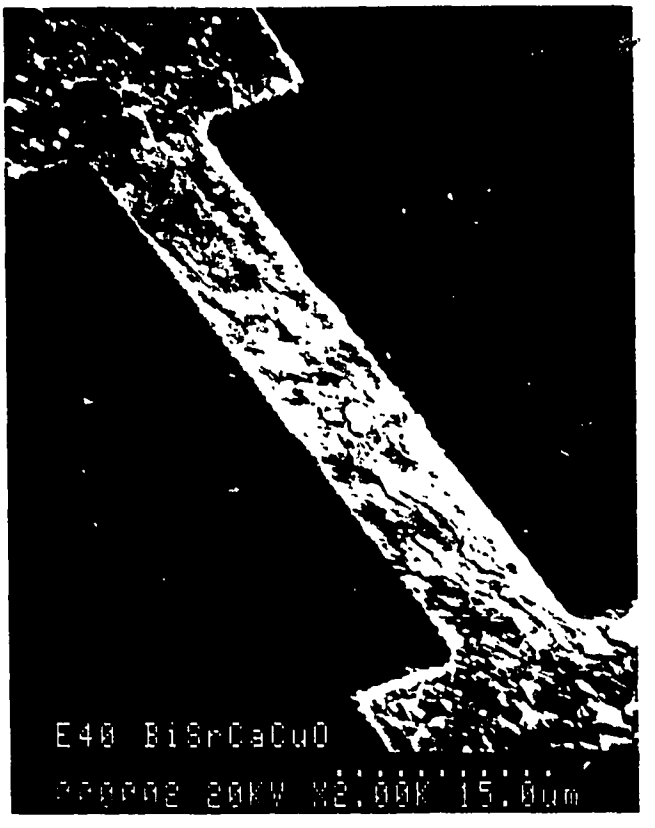

Figure 4.17 - Electron micrograph of BiSrCaCuO line patterned by etching.

for this process is provided by the electron micrograph. A large amount of litter can be found around the film. This material is not present before the heat treatment, and is material that has been deposited during the heat treatment. To solve this problem, films were etched after heat treatment. As the figure shows, the needle-like grains do not appear with this procedure.

Films patterned by these two methods show very different electrical characteristics. The critical current density, J_c in the etched films is very high. We have measured J_c as high as 5×10^5 A/cm^2 at 4 K in these films. Also the zero resistance temperature has been measured as high as 84 K. These properties approach the best measured in $Bi_2Sr_2CaCu_2O_8$. In the films patterned by lift-off, the results are very different. The current density is much lower, typically 10^3 A/cm^2, and the resistive transition is not complete until 77 K.

As Figure 4.18 shows, the current-voltage characteristics are also very different. The etched films show much of the rounding observed in $YBa_2Cu_3O_{7-x}$, but could still be described as "wire-like". The films patterned by lift-off has very different I-V characteristics. These films usually show many discrete, hysteretic switching regions, where the voltage suddenly jumps to a new value. This kind of I-V is reminiscent of that seen in phase-slip centers [62]. Phase-slip centers occur in one dimensional superconductors, where the width and thickness of the wire is less than the coherence length and the penetration depth. Once the critical current is exceeded in the wire, a small normal region appears, and acts as the barrier for a Josephson junction. As the current is increased, more of the regions appear. The appearance of each

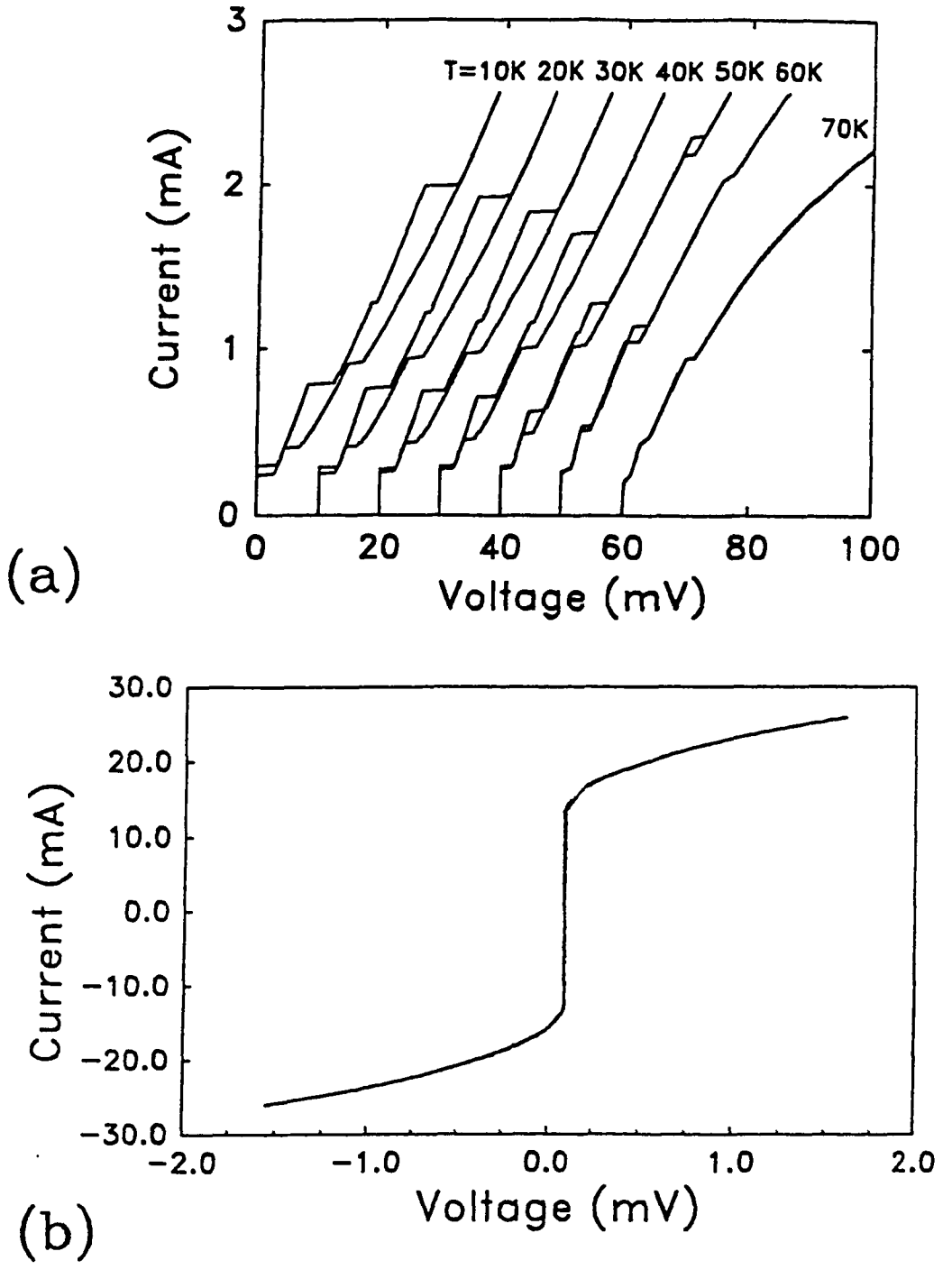

Figure 4.18 - Current-voltage characteristics of BiSrCaCuO lines patterned by (a) lift-off and (b) etching.

of these phase-slips induces a voltage switch in the I-V. This voltage is the sum of voltage increments in series, with each increment characterized by a constant differential resistance. Our samples defy any such analysis. This is not surprising, given what the sample looks like. It seems that this switching behavior must be due to a random arrangement of these needle grains, some in series, and some in parallel. These samples also show very interesting magnetic field behavior, which will be covered in the section on SQUIDs.

4.3.2 *In-Situ* Ion Milling

After successfully fabricating and characterizing wires of $YBa_2Cu_3O_{7-x}$, we wanted to find some systematic way to modify samples and create some controllable Josephson or weak-link behavior [63]. Since the wires were already showing weak-link behavior, we thought that we could isolate some small region of the wire and observe this same behavior in a few grains. To accomplish this we used the ion-milling technique shown in Figure 4.19.

We applied a photoresist etch mask on a patterned wire. This mask was a small window exposing a narrow slot in the wire. The slot was as narrow as we could make it using standard optical lithography (0.8 - 1.0 μm). This photoresist mask then protected the rest of the sample from the Ar ions during ion-milling.

In order to make do systematic studies, we built a liquid-helium-cooled stage for the ion-milling system. This stage also has sixteen electrical feedthroughs, a thermometer, and a heater. We could then do *in-situ* measurements as we milled. The procedure was to mill the sample for some prescribed time, then cool it below its transition temperature

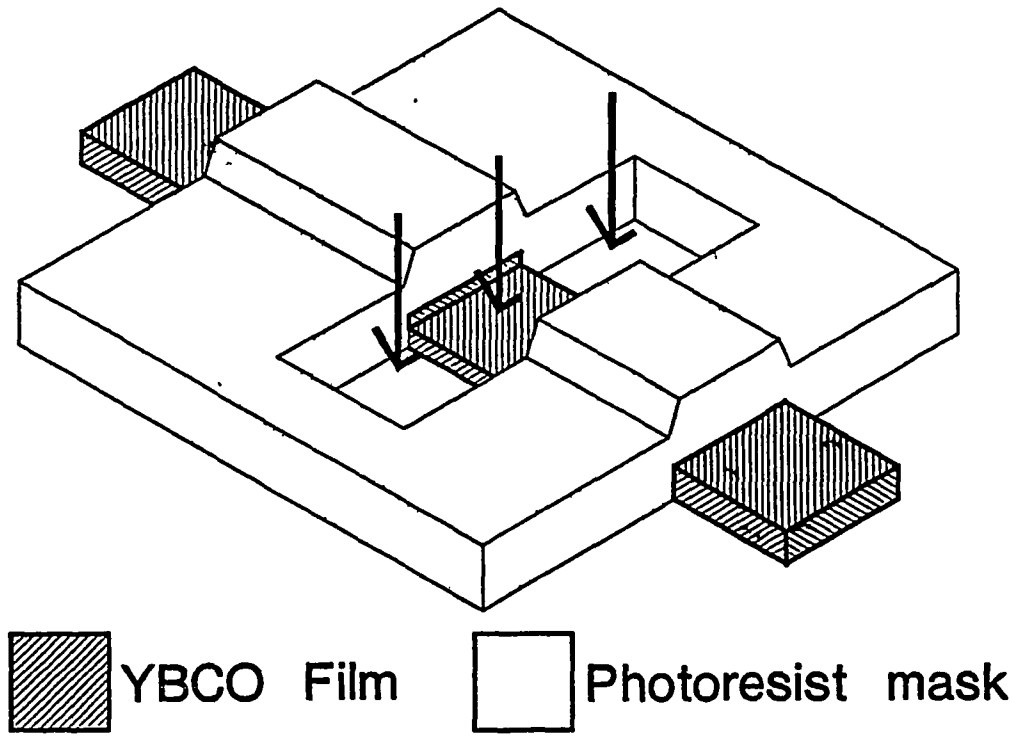

Figure 4.19 - Schematic view of *in-situ* ion milling technique for weak link fabrication.

and measure its properties. We attempted to do the ion-milling on a cold sample, but too much argon condensed on the sample. The sample properties did not change with milling. This suggests that we reached a dynamic equilibrium between argon deposition, and argon removal by the energetic ion beam. Therefore the samples were warmed to above 100 K before milling. We also attempted to monitor the sample during milling when it was warm to see if the small resistance changes could be used as a guide to proper milling time. It turns out that this does not work either. The resistance change of such a small area is small compared with the change of resistance due to heating of the sample by the beam.

We chose to mill at low ion current densities to make the process slow and controllable, and at moderate ion energies to minimize subsurface damage in the exposed portions of the film. At 500 eV ion energies, and a beam current density of 0.3 mA/cm^2 the $YBa_2Cu_3O_{7-x}$ is etched at about 20 nm/minute. This means it takes about 20 minutes to etch entirely through the 400 nm sample.

After each milling operation we made several electrical measurements. These include current-voltage curves, measurements of dynamic resistance *vs.* voltage. In some cases we measured the resistive transition. Figure 4.20 is a typical series of I-V curves for progressively longer milling times. The most obvious change is the decrease in the critical current density. This is expected. It is somewhat surprising that the high voltage resistance does not change more. One possible explanation is that in the unmilled line, the high voltage resistance is a result of J_c being exceeded in a large number of widely distributed grain boundaries, while in the milled line, the area

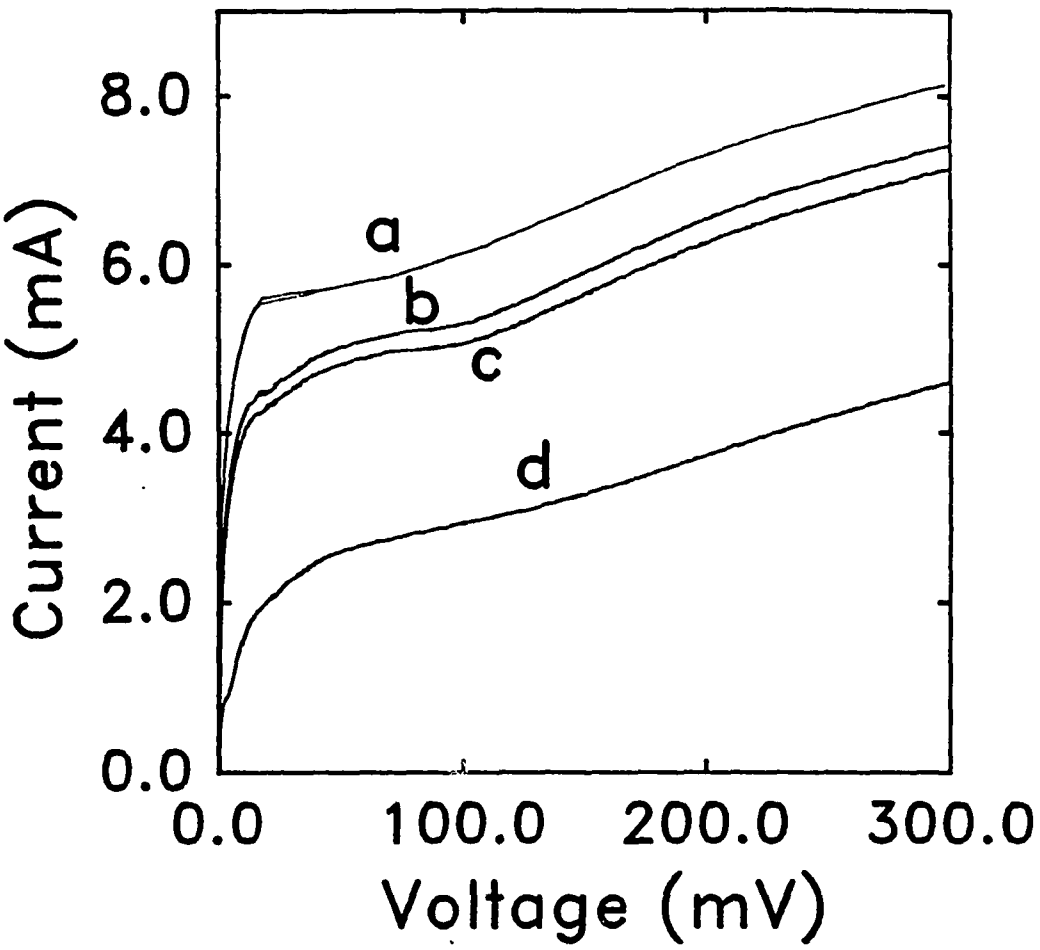

Figure 4.20 - Current-voltage characteristics for ion milled lines: curve (a) unmilled, (b) after 10 min. milling, (c) after 15 min. milling, (d) after 20 min. milling.

is large enough that it behaves much the same, but the cross sectional area is smaller so that J_c is smaller. The most interesting change that occurs as the sample is milled is in the low voltage behavior. Small but definite features appear in the I-V characteristic.

These features are examined best by measuring the dynamic resistance of the sample. We did this using a lock-in technique. Figure 4.21 shows a series of dynamic resistance curves at different temperatures for a milled line. For ease of viewing, each curve has been offset by 100 Ω. The most prominent feature in these curves is a series of dips occurring near 42, 22, and 15 mV, which may be indicative of the energy gap and subharmonics. A gap value of 42 mV give a BCS parameter $2\Delta/k_BT_c$ of 5.4, which is similar to values reported by other groups using methods like Raman scattering and infrared absorption.

Using this method we have also seen I-V characteristics that are very reminiscent of quasiparticle tunneling characteristics. Figure 4.22 show such an I-V. Curves of this type are obtained shortly before the sample is completely milled through, making them difficult to reproduce. If a gap is inferred from this figure, one obtains a value of about 1 mV. It is very unlikely that this value has anything to do with the true gap in the material. The data shown was taken at a temperature of 16 K, and by 25 K all non-linearities have disappeared from the I-V. This leads us to believe that we may be viewing inter-grain tunneling, however the material is so damaged by the milling that both it's gap energy and transition temperature are greatly reduced.

4.3.3 SQUIDs

The first technologically useful devices to be made from high-T_c

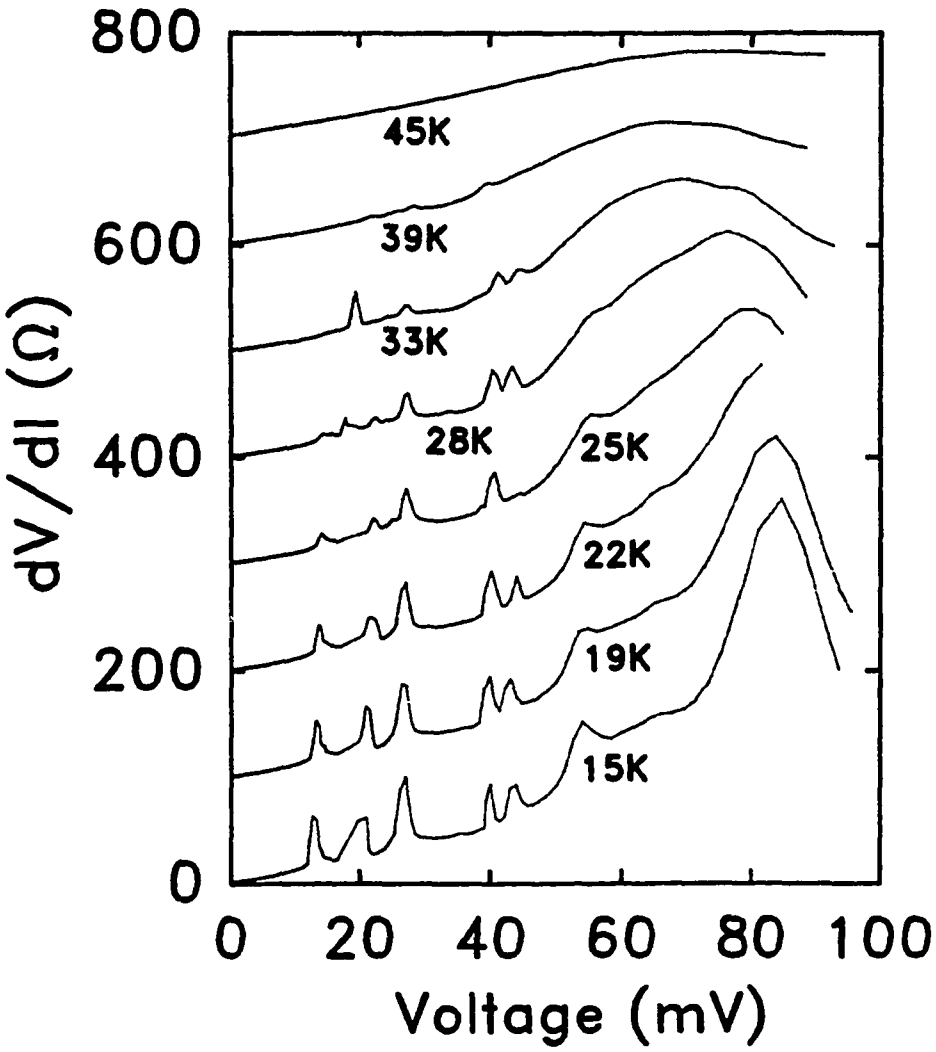

Figure 4.21 - Dynamic resistance *vs.* voltage for a microbridge structure at different temperatures.

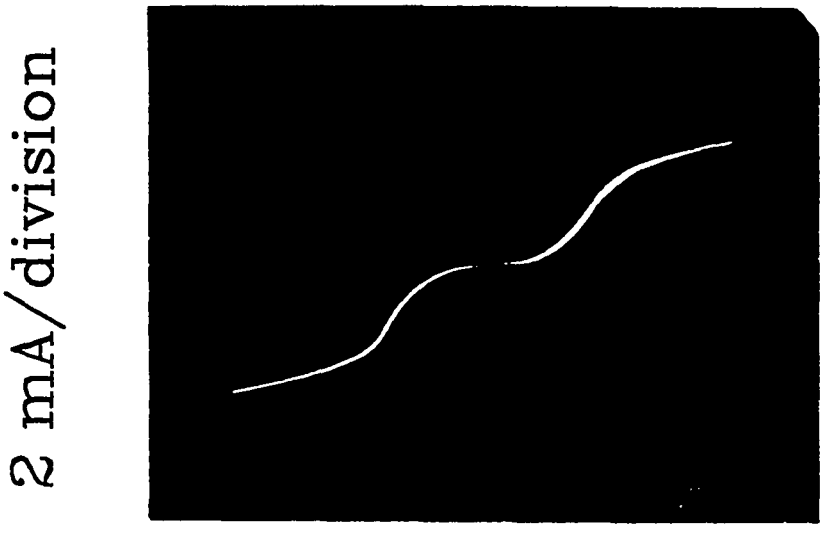

Figure 4.22 -Oscilloscope trace of current-voltage characteristic showing quasiparticle-like tunneling behavior.

superconductors are SQUIDs. This is possible because of the grainy weak-link nature of films. Much like Clarke's SLUG [64], it is possible to make a useful SQUID without having control over the exact nature of the weak links in the SQUID. In all but of a few of the high-T_c SQUIDs, no attempt is made to control the weak-links. A film is deposited in a loop pattern, and the random grain patterns form a structure in which the critical current I_c is modulated by the flux enclosed in the loop, Φ. We took the same approach.

We have patterned both $YBa_2Cu_3O_{7-x}$ and $Bi_2Sr_2CaCu_2O_8$ films into loop geometries. In most of these films we saw no modulation. One explanation is the lack of magnetic shielding in our high-temperature cryostat. Typically the flux sensitivity in these grainy SQUIDs is small, about 10 $\mu V/\Phi_0$. Without good magnetic shielding, the modulation can be difficult to detect. Also our geometry differs from other groups. Our loops are connected to relatively long thin wires, while most other groups have very large solid regions with small SQUID loops in between. As we will show, it is possible to get a flux modulation from a single grainy wire. It is possible that many small flux modulation signals from the grains in series masks the modulation due to the loop.

As mentioned earlier, the BiSrCaCuO lines that we patterned by lift-off show a strong magnetic field behavior. Many of them operate as very sensitive SQUIDs. We attribute this behavior to the very weak coupling between the random needle grains in these lines. A plot of voltage *vs.* applied flux for one of these lines is shown in Figure 4.23. From the size of the field applied, we can infer that the effective loop area is about $(10\ \mu m)^2$. This value is consistent with the grain sizes of

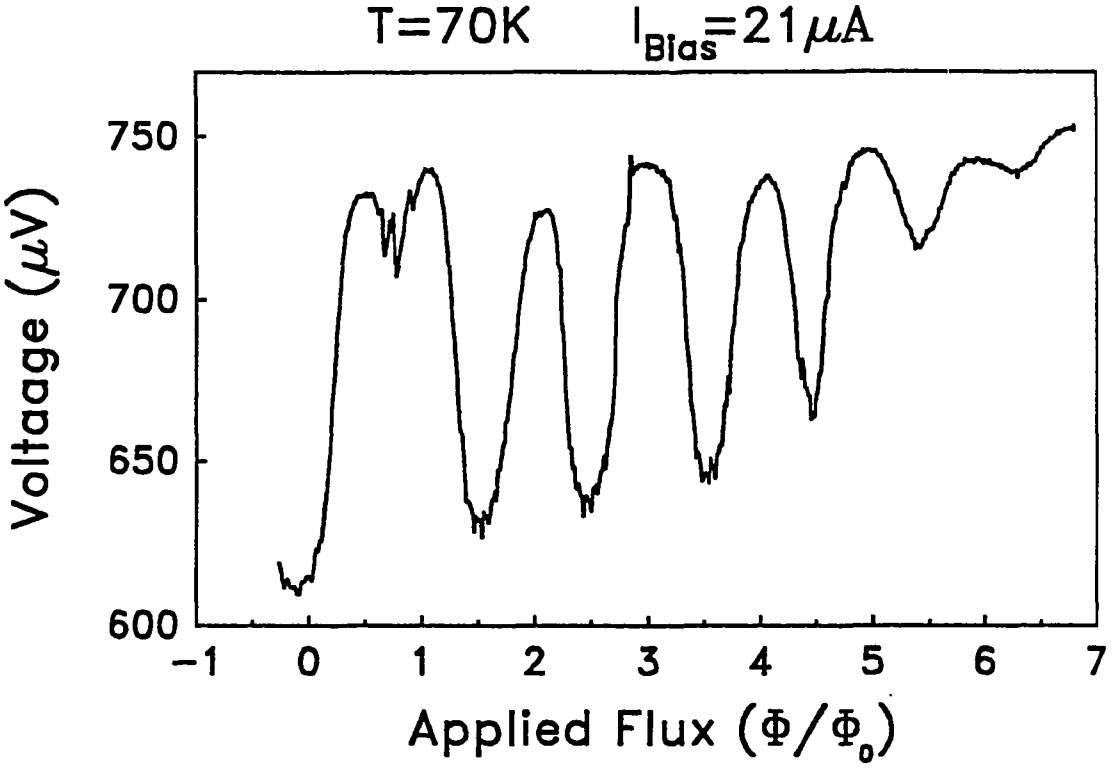

Figure 4.23 - Voltage *vs.* applied flux for a BiSrCaCuO SQUID.

the film shown in Figure 4.16. The most striking feature of these SQUIDs is their large flux sensitivity, $dV/d\Phi = 700\ \mu V/\Phi_0$. This is the largest value yet reported in a SQUID made from high-T_c superconductors. We attain this large flux sensitivity at temperatures as high as 75 K. However, these devices are not without their flaws. They must be operated at high temperatures, because of the hysteresis in the I-V characteristic. It may be possible to remove this hysteresis by resistively shunting the SQUIDs. Also, like most other high-T_c SQUIDs, these devices show magnetic hysteresis. The V-Φ curve does not retrace itself exactly as the field is increased and decreased. This is due to the motion of unpinned vortices in the SQUID. Lastly, because of flux flow, and the uncontrolled nature and number of weak links, these devices show non-ideal V-Φ modulation. Typically they only modulate with a fixed period for a few flux quantum. As more field is applied, different configurations of the grains also modulate as SQUIDs, washing out the overall modulation. Figure 4.23 shows another interesting phenomenon. A SQUID should show minimum voltage at integer applied flux quanta. In this curve, there is a minimum at zero flux, but all other minima are at half-integer flux quanta. In this sample the curve seems to "slip". This phenomena has been observed in other SQUIDs and at different places on the V-Φ curve, both on forward trace and retrace. The point at which the slip occurs is well defined and repeatable. This behavior is a more dramatic example of the magnetic hysteresis discussed above. We feel that the "slips" are due to flux trapping and the random nature of the grains making up the SQUID, perhaps causing a configurational change of the grains acting as the SQUID. Although these SQUIDs have many obvious

problems, devices with these kind of characteristics are good candidates for technological application. They can be operated at very high temperatures, and are very sensitive. In practical operation, the magnetic hysteresis and "slipping" are not a problem. SQUIDs are normally operated in a flux locked manner, where they are biased at a fixed flux, and maintained at that point by a feedback circuit.

Chapter 5

SUMMARY AND FUTURE DIRECTIONS

We have performed experiments in two very different fields of superconductivity. In the first, we verified a previously predicted effect, the generation of a charge imbalance by the interaction of an electric field and a supercurrent. We have measured the temperature dependence of this effect, and found that in our samples, and in the temperature range measured that it has a $(1 - T/T_c)$ dependence. This result is not in agreement with existing theory, however these calculations were carried out in the clean limit, and our samples were in the dirty limit. We are confident that our observations are of the predicted effect, because of the bi-linearity of the generated charge imbalance in both electric field and supercurrent.

The second group of experiments were performed in the field of high-T_c superconductivity. We have fabricated thin films of YBaCuO by multiple-source deposition and pulsed-laser deposition and BiSrCaCuO by sequential evaporation. In all cases we were able to fabricate films of good quality. We have explored ways of patterning these films into microelectronic structures, and made simple transport measurements on these structures. We developed an *in-situ* modification technique that allowed us to systematically modify thin films in hopes of enhancing grain boundary effects. This technique, while yielding no definitive results, produced results indicative of tunneling between grains and

showed possible evidence for an energy gap. We also produced SQUIDs based on inter-grain coupling in some of our films. These SQUIDs have the highest flux-voltage sensitivity of any high-T_c SQUID yet reported.

There are many interesting ways to extend this work. The non-equilibrium experiment, while clearly showing the effect that was sought, leaves many questions unanswered. It would be very interesting to perform this experiment in the clean limit. Practically, this is unlikely. It is very difficult to make aluminum films that will be in the clean limit near T_c. It might be possible to perform similar experiments in other materials, but the large quasiparticle diffusion length in aluminum makes it the ideal choice. Alternatively, extending this work to study the impurity dependence might be as interesting as clean limit measurements. There are many other non-equilibrium experiments yet to be done. Most of the off-diagonal terms of Eq. (3.1) have yet to be studied. Perhaps they will yield similar surprises.

In the field of high-temperature superconductivity, the prospects for future work are much clearer. The number of researchers in this field is still enormous. In thin film work, the advent of pulsed laser deposition has created much excitement. With this technique it should be possible to grow films with very clean interfaces, and perhaps even make "real" tunnel junctions. Many groups (including ours) are currently addressing this problem. Recently, Gurvitch *et al.* [65] has found a way to make repeatable tunnel junctions on single crystals of YBaCuO. This is a very exciting result, and should lead the way to much future work.

There are also a class of experiments that combine some of the ideas of both parts of this thesis. The suspected large anisotropy of the gap

in the high-T_c materials can lead to an anomalously large thermoelectric effect if the thermal gradient is not applied along a principal crystal direction [66]. In this situation, the supercurrent and normal currents do not exactly cancel each other. These experiments are simpler in some ways than those we performed, because they do not require high-quality tunneling probes. It has also been suggested that these experiments could elucidate the nature of the pairing in these superconductors.

REFERENCES

1. J. Bardeen, L. N. Cooper, and J. R. Schrieffer, Phys. Rev. **108**, 1157 (1957).

2. L. N. Cooper, Phys. Rev. **104**, 1189 (1956).

3. N. N. Bogoliubov, Soviet Phys. - JETP **7**, 41 (1958).

4. M. Tinkham, Introduction to Superconductivity, (McGraw-Hill, New York, 1975).

5. M. Cyrot, Rep. Prog. Phys. **36**, 103 (1973).

6. B. D. Josephson, Phys. Lett. **1**, 251 (1962).

7. V. Ambegaokar and A. Baratoff, Phys. Rev. Lett. **10**, 486 (1963).

8. A. Baratoff, J. A. Blackburn, and B. B. Schwartz, Phys. Rev. Lett. **25**, 1096 (1970).

9. D. E. McCumber, J. Appl. Phys. **39**, 3113 (1968).

10. W. C. Stewart, Appl. Phys. Lett. **12**, 277 (1969).

11. C. J. Pethick and H. Smith, Ann. Phys. **119**, 133 (1979).

12. Albert Schmid, J. Low Temp. Phys. **41**, 37, (1980).

13. J. Clarke, B. R. Fjordbøge, and P.E. Lindelof, Phys. Rev. Lett. **43**, 642, (1979).

14. D. J. Van Harlingen, Physica, **109 & 110B**, 1710, (1982).

15. H. Jonathon Mamin, John Clarke, and D. J. Van Harlingen, Phys. Rev. B **29**, 3881, (1984).

16. A. Schmid and G. Schön, J. Low Temp. Phys. **20**, 207, (1975).

17. M. Tinkham, Phys Rev. B **6**, 1747 (1972).

18. T. R. Lemberger, Phys. Rev. B **29**, 4946 (1984).

19. C. C. Chi and John Clarke, Phys. Rev. B **19**, 4495 (1979).

20. Thomas R. Lemberger and John Clarke, Phys. Rev. B **23**, 1088, (1981).

21. Thomas R. Lemberger and John Clarke, Phys. Rev. B **23**, 1100, (1981).

22. R. T. Wakai, Ph.D. thesis, University of Illinois, 1987.

23. Mark Johnson and R. H. Silsbee, Phys. Rev. Lett. **58**, 2806 (1987)

24. A. W. Sleight, J. L. Gillson, and P. E. Bierstedt, Solid State Commun. 17, 27 (1975).

25. J. G. Bednorz and K. A. Müller, Z. Phys. B 64, 189 (1986).

26. M. K. Wu, J. R. Ashburn, C. T. Torng, P. H. Hor, R. L. Meng, L Gao, Z. J. Huang, Y. Q. Wang and C. W. Chu, Phys. Rev. Lett. 58, 908 (1987).

27. H. Maeda, Y. Tanaka, M. Fukutumi and T. Asano, Jap. J. Appl. Phys. 27, L209 (1988).

28. Z. Z. Sheng and A. M. Hermann, Nature 332, 55 (1988).

29. L. F. Matteiss, E. M. Gyorgy, and D. W. Johnson Jr., Phys. Rev. B 37, 3745 (1988).

30. Y. Tokura, H. Takagi, and S. Uchida, Nature 337, 345 (1989).

31. Donald M. Ginsberg, editor Physical Properties of High Temperature Superconductors I, (World Scientific, Singapore, 1989).

32. P. Chaudhari, R. H. Koch, R. B. Laibowitz, T. R. McGuire and R. J. Gambino, Phys. Rev. Lett. 58, 2684 (1987).

33. M. Naito, R. H. Hammond, B. Oh, M. R. Hahn, J. W. P. Hsu, P. Rosenthal, A. F. Marshal, M. R. Beasley, T. H. Geballe and A. Kapitulnik, J. Mater. Res. 2, 713 (1987).

34. Y. Enomoto, T. Murakami, M. Suzuki and K. Moriwaki, Jpn. J. Appl. Phys. 26, L1248 (1987).

35. T. Aida, T. Fukazawa, M. Suzuki, and K. Moriwaki, Jpn. J. Appl. Phys. 26, L1481 (1987).

36. K. Char, A. D. Kent, A. Kapitulnik, M. R. Beasley, and T. H. Geballe, Appl. Phys. Lett. 51, 1370 (1987).

37. M. Scheuermann, C. C. Chi, C. C. Tsuei, D. S. Yee, J. J. Cuomo, R. B. Laibowitz, R. H. Koch, B. Braren, R. Srinivasan, and M. M. Plechaty, Appl. Phys. Lett. 51, 1951 (1987).

38. J. Gao, Y. Z. Zhang, B. R. Zhao, P. Out, C. W. Yuan, and L. Li, Appl. Phys. Lett. 53, 2675 (1988).

39. X. D. Wu, A. Inam, T. Vanketesan, C. C. Chang, E. W. Chase, P. Barboux, J. M. Tarascon and B. Wilkens, Appl. Phys. Lett. 52, 754 (1988).

40. C. E. Rice, R. B. van Dover and G. J. Fisanick. Appl. Phys. Lett. 51, 1842 (1987).

41. S. Kramer, G. Kordas, J. McMillan, G. C. Hilton and D. J. Van Harlingen, Appl. Phys. Lett. **53**, 156 (1988).

42. A. Mogro-Campero and L. G. Turner, Appl. Phys. Lett. **52**, 1185 (1988).

43. P. M. Mankiewich, J. H. Scofield, W. J. Skocpol, R. E. Howard, A. H. Dayem and E. Good, Appl. Phys. Lett. **51**, 1753 (1987).

44. Siu Wan Chan, B. G. Bagley. L. H. Greene, M. Giroud, W. L Feldmann, K. R. Jenkin II and B. J. Wilkins, Appl. Phys. Lett.

45. R. M. Silver, A. B. Berezin, M. Wendman, and A. L. de Lozanne, Appl. Phys. Lett. **52**, 2174 (1988).

46. D. K. Lathrod, S. E. Russek, and R. A. Buhrman, Appl. Phys. Lett. **51**, 1554 (1987).

47. D. D. Berkley, B. R. Johnson, N. Anand, K. M. Beauchamp, L. E. Conroy, A. M. Goldman, K. Mauersberger, M. L. Mecartney, J. Morton, M. Tuominen, and Y-J. Zhang, Appl. Phys. Lett. **53**, 1973 (1988).

48. T. Terashima, K. Iijima, K. Yamamoto, Y. Bando, and H. Mazaki, Jpn. J. Appl. Phys. **27**, L91 (1988)

49. Osamu Michikami, Masaayoshi Ashai, and Hidefumi Asano, Lpn. J. Appl. Phys. **28**, L448 (1989).

50. D. M. Hwang, T. Vanketesan, C. C. Chang, L. Nazar, X. D. Wu, A Inam, and M. S. Hegde, Appl. Phys. Lett. **54**, 1702 (1989).

51. R. H. Koch, C. P. Umbach, G. J. Clark, P. Chaudhari and R. B. Laibowitz, Appl. Phys. Lett. **51**, 200 (1987).

52. B Häuser, M. Diegel and H. Rogalla, Appl. Phys. Lett. **52**, 844 (1988).

53. P. Chaudhari, J. Mannhart, D. Dimos, C. C. Tsuei, J. Chi, M. M. Oprysko amd M. Scheuermann, Phys. Rev. Lett. **60**, 1653 (1988).

54. M. Lee, M. Naito, M. R. Beasley, and A. Kapitulnik, Bull. Am. Phys. Soc. **33**, 594 (1988).

55. P. M. Mankiewich, D. B. Schwartz, R. E. Howard, L. D. Jackel, B. L. Straughn, E. G. Burkhardt, A. H. Dayem, SPIE Proc. **948**, 37 (1988).

56. B. Y. Tsaur, M. S. Diorio, and A. J. Strauss, Appl. Phys. Lett. **51**, 858 (1987).

57. A. Mogro-Campero, B. D. Hunt, L. G. Turner, M. C. Burrell, and W. E. Balz, Appl. Phys. Lett. **52**, 584 (1988).

58. G. Koren, A. Gupta, E. A. Giess, A. Segmuller, and R. B. Laibowitz, Appl. Phys. Lett. **54**, 1054 (1989).

59. T. Vanketesan, X. D. Wu, A. Inam, and J. B. Wachtman, Appl. Phys. Lett. **52**, 1193 (1988).

60. K. N. Springer and D. J. Van Harlingen, Phys. Rev. B **36**, 7273 (1987).

61. D. J. Van Harlingen, K. N. Springer, G. C. Hilton, and J. Tien, Physica **152B**, (1988).

62. W. J. Skocpol, in Nonequilibrium Superconductivity, Phonons, and Kapitza Boundries, NATO ASI Series B: Physics, Vol. 65, ed. K. E. Gray, Plenum, New York (1981), p. 559.

63. G. C. Hilton, E. B. Harris, and D. J. Van Harlingen, Appl. Phys. Lett. **53**, 1107 (1988).

64. J. Clarke, Phil. Mag. **13**, 155 (1966).

65. M. Gurvitch, J. M. Valles, Jr., A. M. Cucolo, R. C. Dynes, J. P. Garno, L. F. Schneemeyer, and J. V. Waszczak, submitted to Phys. Rev. Lett.

66. B. Arfi, H. Bahlouli, C. J. Pethick, and David Pines, Phys. Rev. Lett. **60**, 2206 (1988).

VITA

Gene Charles Hilton was born April 22, 1959 in Freeport, New York. After graduation from high school in a suburb of Chicago, Illinois, he attended the University of Tulsa in Tulsa, Oklahoma, graduating with a B.S. in engineering physics in 1981.